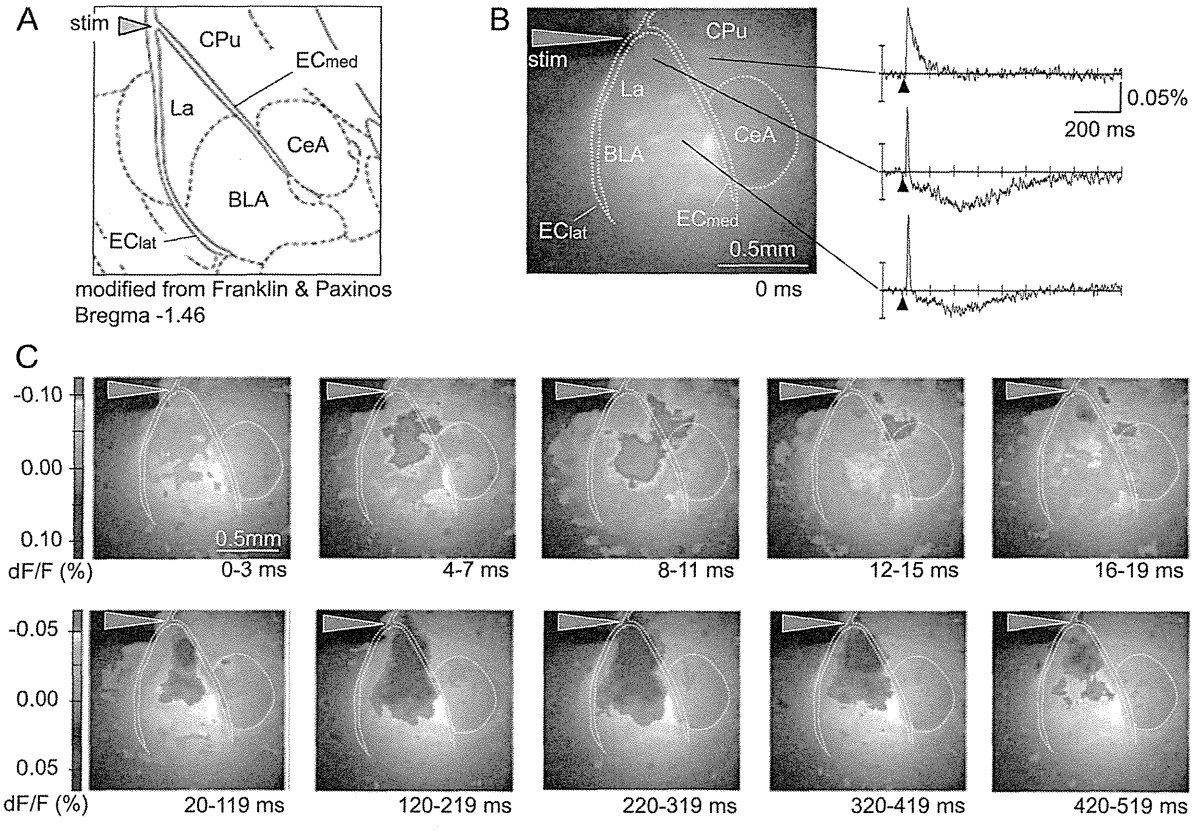

Fig. 1. Optical signal propagation after the EC stimulation.
(A) The modified schematic diagram from the atlas of Franklin and Paxinos (2007) at Bregma −1.46 mm. The arrowhead shows the ramifying point of the external capsule (EC); lateral branch of the external capsule (EClat) and medial branch of the external capsule (ECmed). La – lateral amygdala nucleus; BLA – basolateral amygdala nucleus; CeA – central amygdala nucleus; CPu – caudate putamen. (B) Left, the fluorescence image of VSD-stained coronal slice. Right, a typical example of optical signals in the CPu (in the top wave), La (in the middle wave) and BLA (in the bottom wave). Brown arrowhead, the stimulating site; black arrowhead, the timing of electrical stimulation. (C) Images of optical signal changes produced at the various indicated times after electrical stimulation. In the upper panels, images for 4 frames were stacked to show the spread pattern of depolarization. In the lower panels, images for 100 frames were stacked to show the spread pattern of hyperpolarization.

during the following 100 ms (120–219 ms). The maximal hyperpolarization was observed in the La along the dorsal part of the ECmed from 220 to 319 ms. The strong and long-lasting hyperpolarization was mainly observed in the La (the middle wave in Fig. 1B), while the hyperpolarization in the BLA was weak (the bottom wave). The hyperpolarization was neither observed in the main part of the CPu (the top wave) nor in the CeA, while the depolarization in the CPu lasted longer than in the La and the BLA.

3.2. *Effects of the deafferentation on the optical signals*

To reveal the afferent pathway responsible for evoking the strong and long-lasting hyperpolarization, effects of the various surgical operations were investigated.

Deafferentation from the EClat to the La did not affect the induction of the strong and long-lasting hyperpolarization in the La (Fig 2A), and there was no significant change in the OI value compared with the sham (Fig. 2E), suggesting that the afferent inputs via the EClat are not involved in the hyperpolarization induced in the La. In contrast, deafferentation from the ECmed to the La strongly reduced the hyperpolarization (Fig. 2B). OI values were also significantly reduced (Fig. 2E). These results suggest that the inputs via the ECmed are involved in the hyperpolarization induced in the La.

Next, to investigate the involvement of inputs from the main part of the CPu, we cut off the input from the CPu to the ECmed. In this experiment, the connections between the ECmed and the La remained. The OI values after deafferentation did not significantly change (Fig. 2C and E), suggesting that the inputs from the CPu are not involved in the hyperpolarization induced in the La. For further investigation of the inputs via ECmed, a transverse cut at the dorsal part of the ECmed was carried out. As a result, the hyperpolarization was significantly reduced in the La (Fig. 2D). These data suggest that the fibers running along the ECmed were involved in the induction of hyperpolarization.

3.3. *Effects of glutamatergic antagonists and the source of the inhibition*

Finally, to confirm the details of the inhibitory input source and its properties, the effects of glutamatergic antagonists (6-cyano-7-nitroquinoxaline-2,3-dione (CNQX, 10 μM, TOCRIS), D-(−)-2-amino-5-phosphonopentanoic acid (D-AP5, 50 μM, TOCRIS)) on the inhibitory responses were investigated. The inhibitory responses in the La induced by EC stimulation were statistically significantly reduced after the application of glutamatergic antagonists (Fig. 3A), suggesting that excitatory glutamatergic inputs were involved in the inhibitory response.

We then stimulated several parts along the ECmed in the presence of glutamatergic antagonists (Fig. 3B). Stimulation at the dorsal part of the ECmed did not induce the hyperpolarization (Fig. 3Ba); however, the hyperpolarization could be induced when the middle part of the ECmed was stimulated (Fig. 3Bb). When the electrode moved to the ventral part of the ECmed, weak hyperpolarizing responses were observed (Fig. 3Bc). The magnitude of the hyperpolarization induced by the stimulation at the middle part of the ECmed was statistically significantly larger than that induced by

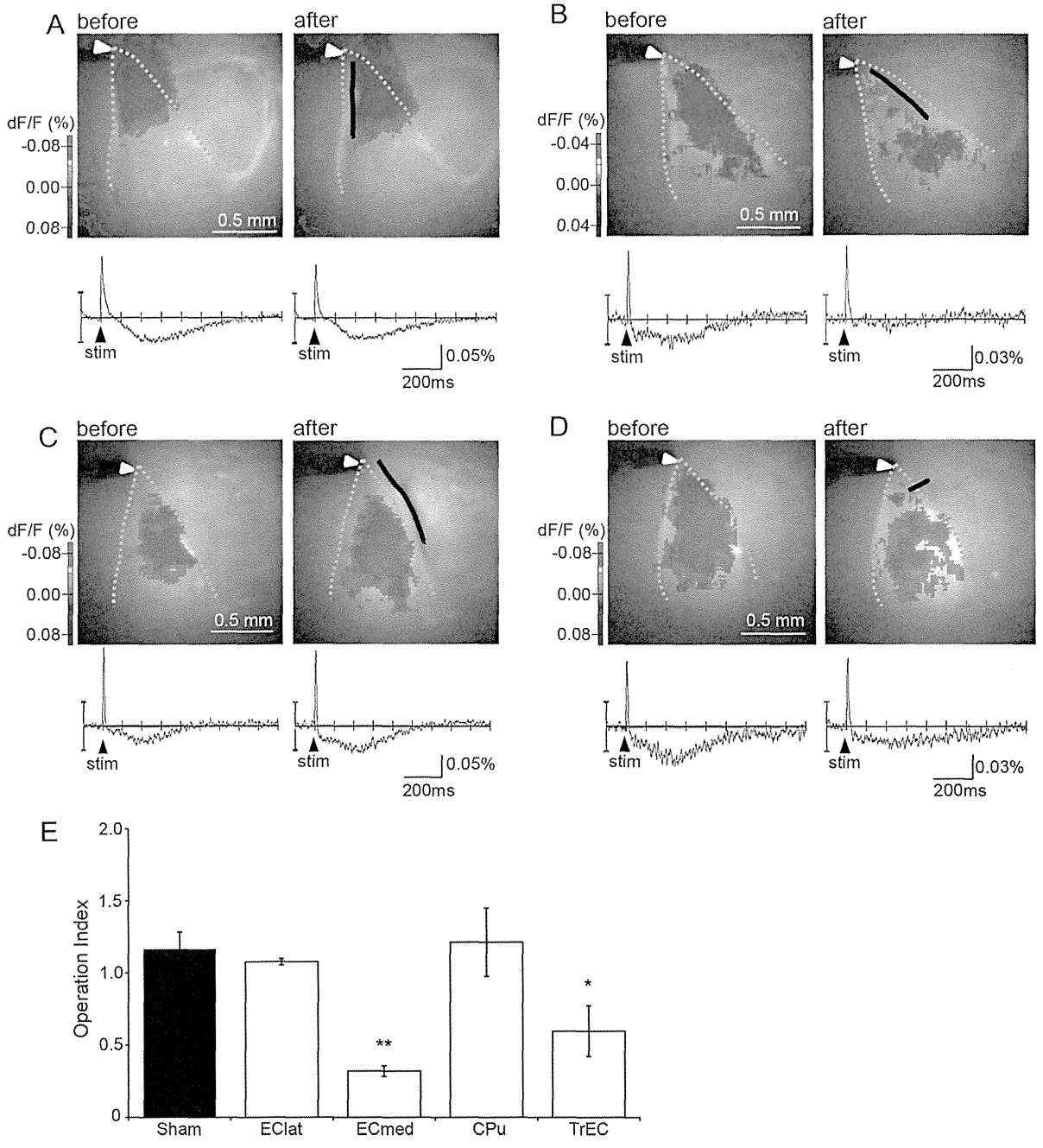

Fig. 2. Effects of deafferentation of the lateral amygdala nucleus on the inhibitory responses.
(A–C) Afferent pathways to the lateral amygdala nucleus were surgically cut from the lateral branch of the external capsule (EClat) in (A), the medial branch (ECmed) in (B), and the caudate putamen (CPu) in (C) to the La was performed, respectively. Black lines, the surgical cut sites; white arrowhead, the stimulating site. The upper images of panels A, B, and C show the spread pattern of hyperpolarization before and after operation. Lower traces, the optical signal traces; black arrowhead, the timing of electrical stimulation. (D) The dorsal part of the ECmed was cut transversely (TrEC). (E) Operation indices (OIs) were quantitatively analyzed among various deafferentations. OIs of ECmed ($n = 6$ slices from 6 mice) and TrEC ($n = 7$ slices from 4 mice) were significantly lower than those of Sham ($n = 5$ slices from 3 mice), EClat ($n = 5$ slices from 4 mice), and CPu ($n = 7$ slices from 4 mice). $^{*}p < 0.05$; $^{**}p < 0.01$.

the stimulation at the other parts (Fig. 3Bd). These results suggest that inhibitory neurons located in the middle part of the ECmed are the main source of the hyperpolarization in the La.

4. Discussion

VSD imaging is a powerful tool to investigate spatial and temporal patterns in the propagation of membrane potential change in the brain tissue. Furthermore, optical signals from the stained slice preparation with VSD are reported to be well-correlated to field EPSPs in vitro [7,8,10,19,25,29,32]. In the amygdala, the signal propagations from the La to the BLA [35,36] and from the La to the CeA have been visualized using VSD imaging [3]. However, these previous studies focused on the propagation of depolarizing signals in the amygdala but not of hyperpolarizing signals.

In the present study, we demonstrated the propagation of the inhibitory responses in the amygdala formation using VSD imaging. The strong and long-lasting hyperpolarization is evoked in the La after the sharp and strong depolarization. In addition, the surgical-cut and the pharmacological experiments indicate that the source of the inhibitory responses is not located in the La or the CPu, but is located in the middle part of the ECmed. According to this

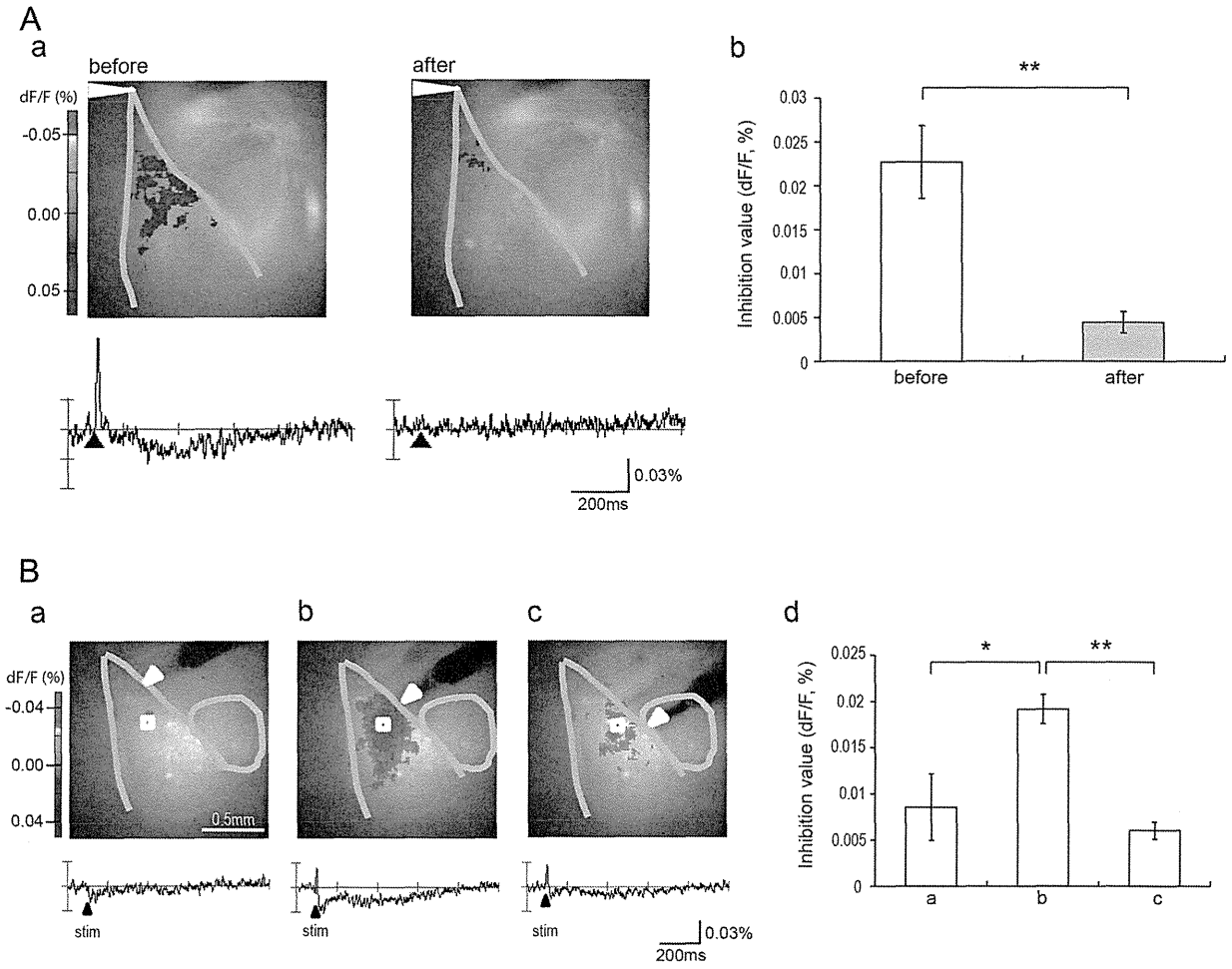

Fig. 3. Effects of glutamatergic antagonists on the inhibitory responses.
(A) The effects of glutamatergic antagonists (CNQX + D-AP5) on the inhibitory response induced by the stimulation of the ramifying point of the external capsule. (Aa) Left and right upper images indicate the spread pattern of hyperpolarization before and after the drug application, respectively. White arrowhead, the stimulating site; lower traces, the optical signal traces; black arrowhead, the timing of electrical stimulation. (Ab) Inhibitory value was statistically compared between before and after CNQX + D-AP5 application ($n = 5$ slices from 5 mice; $^{**}p < 0.01$). (B) The dependence of the stimulus position on inhibitory response of the La in the presence of CNQX + D-AP5. (Ba–c) Upper images indicate the spread pattern of hyperpolarization when the stimulus electrode was at the dorsal, middle, and ventral part of the ECmed, respectively. White arrowhead, the stimulating site; lower traces, the optical signal traces; white squares, the area of which the traces were calculated; black arrowhead, the timing of electrical stimulation. (Bd) Inhibitory value was shown when the stimulus electrode was at the dorsal (a), middle (b), and ventral (c) part of the ECmed ($n = 4$ slices from 4 mice; $^{*}p < 0.05$; $^{**}p < 0.01$).

anatomical location, the source of the inhibitory inputs is likely from the m-ITC in the ECmed [5,18,20,27]. The inhibitory responses were completely eliminated in the presence of the glutamatergic antagonists, indicating that the inhibitory responses are based on the glutamatergic input passing through ECmed. Furthermore, local stimulation of the middle part of the ECmed produces inhibitory responses even in the presence of glutamatergic antagonists, suggesting that GABAergic neurons in the m-ITC are the source of the inhibitory responses of the La. A TrEC cut results in a smaller reduction of the inhibitory responses than an ECmed cut. Because it has been reported that stimulation of the La and the BLA excites the m-ITC neurons [27,28], excitatory glutamatergic inputs to the m-ITC through the La and the BLA might be involved in the inhibitory response in addition to the glutamatergic inputs coming along the ECmed.

In the present study, the contribution of the lateral intercalated clusters located in the EClat was smaller than that of the m-ITC, although the pathway from the lateral intercalated clusters to the BLA has been shown anatomically and electrophysiologically [16,30]. Because the direction of the stimulus electrode used in the present study was from the EClat to the ECmed, resulting in the selective stimulation of the ECmed, the contribution of the lateral intercalated clusters to the inhibitory response in vivo cannot be excluded.

It has been reported that the stimulation of the La and the BLA excites the m-ITC neurons [27,28], resulting in the inhibition of the CeA neurons [2,27]. This pathway is suggested to be involved in the fear extinction mechanism [1], while the inhibitory inputs from m-ITC to La might interfere with the acquisition of fear memory.

In summary, the present study demonstrates the spatial and temporal spread pattern of the inhibitory response in the La after the stimulation of the EC using VSD imaging. Moreover, it is indicated that the inhibitory response is induced via the m-ITC. The pathway from the m-ITC to the La might have inhibitory effects on the acquisition of fear memory.

Acknowledgements

We thank Drs. Miwa and Shimizu for their support. This work was supported by Research Grants from MHLW.

References

[1] T. Amano, C.T. Unal, D. Pare, Synaptic correlates of fear extinction in the amygdala, Nat. Neurosci. 13 (2010) 489–494.
[2] A. Amir, T. Amano, D. Pare, Physiological identification and infralimbic responsiveness of rat intercalated amygdala neurons, J. Neurophysiol. 105 (2011) 3054–3066.
[3] C. Avrabos, S.V. Sotnikov, J. Dine, P.O. Markt, F. Holsboer, R. Landgraf, M. Eder, Real-time imaging of amygdalar network dynamics in vitro reveals a neurophysiological link to behavior in a mouse model of extremes in trait anxiety, J. Neurosci. 33 (2013) 16262–16267.
[4] E.P. Bauer, J.E. LeDoux, Heterosynaptic long-term potentiation of inhibitory interneurons in the lateral amygdala, J. Neurosci. 24 (2004) 9507–9512.
[5] D. Busti, R. Geracitano, N. Whittle, Y. Dalezios, M. Manko, W. Kaufmann, K. Satzler, N. Singewald, M. Capogna, F. Ferraguti, Different fear states engage distinct networks within the intercalated cell clusters of the amygdala, J. Neurosci. 31 (2011) 5131–5144.
[6] I. Ehrlich, Y. Humeau, F. Grenier, S. Ciocchi, C. Herry, A. Luthi, Amygdala inhibitory circuits and the control of fear memory, Neuron 62 (2009) 757–771.
[7] A. Grinvald, L.B. Cohen, S. Lesher, M.B. Boyle, Simultaneous optical monitoring of activity of many neurons in invertebrate ganglia using a 124-element photodiode array, J. Neurophysiol. 45 (1981) 829–840.
[8] A. Grinvald, A. Manker, M. Segal, Visualization of the spread of electrical activity in rat hippocampal slices by voltage-sensitive optical probes, J. Physiol. 333 (1982) 269–291.
[9] T. Iijima, M.P. Witter, M. Ichikawa, T. Tominaga, R. Kajiwara, G. Matsumoto, Entorhinal-hippocampal interactions revealed by real-time imaging, Science 272 (1996) 1176–1179.
[10] W. Jin, R.J. Zhang, J.Y. Wu, Voltage-sensitive dye imaging of population neuronal activity in cortical tissue, J. Neurosci. Methods 115 (2002) 13–27.
[11] M.Z. Kee, J.P. Wuskell, L.M. Loew, G.J. Augustine, Y. Sekino, Imaging activity of neuronal populations with new long-wavelength voltage-sensitive dyes, Brain Cell Biol. 36 (2008) 157–172.
[12] N. Koganezawa, A. Taguchi, T. Tominaga, S. Ohara, K. Tsutsui, M.P. Witter, T. Iijima, Significance of the deep layers of entorhinal cortex for transfer of both perirhinal and amygdala inputs to the hippocampus, Neurosci. Res. 61 (2008) 172–181.
[13] J.E. LeDoux, Emotion circuits in the brain, Annu. Rev. Neurosci. 23 (2000) 155–184.
[14] J.E. LeDoux, P. Cicchetti, A. Xagoraris, L.M. Romanski, The lateral amygdaloid nucleus: sensory interface of the amygdala in fear conditioning, J. Neurosci. 10 (1990) 1062–1069.
[15] D. Marcellino, M. Frankowska, L. Agnati, M. Perez de la Mora, V. Vargas-Barroso, K. Fuxe, J. Larriva-Sahd, Intercalated and paracapsular cell islands of the adult rat amygdala: a combined rapid-Golgi, ultrastructural, and immunohistochemical account, Neuroscience 226 (2012) 324–347.
[16] A. Marowsky, Y. Yanagawa, K. Obata, K.E. Vogt, A specialized subclass of interneurons mediates dopaminergic facilitation of amygdala function, Neuron 48 (2005) 1025–1037.
[17] A.J. McDonald, Neurons of the lateral and basolateral amygdaloid nuclei: a Golgi study in the rat, J. Comp. Neurol. 212 (1982) 293–312.
[18] O.E. Millhouse, The intercalated cells of the amygdala, J. Comp. Neurol. 247 (1986) 246–271.
[19] M. Nakamura, Y. Sekino, T. Manabe, GABAergic interneurons facilitate mossy fiber excitability in the developing hippocampus, J. Neurosci. 27 (2007) 1365–1373.
[20] L. Nitecka, Y. Ben-Ari, Distribution of GABA-like immunoreactivity in the rat amygdaloid complex, J. Comp. Neurol. 266 (1987) 45–55.
[21] H.C. Pape, D. Pare, Plastic synaptic networks of the amygdala for the acquisition, expression, and extinction of conditioned fear, Physiol. Rev. 90 (2010) 419–463.
[22] D. Pare, G.J. Quirk, J.E. Ledoux, New vistas on amygdala networks in conditioned fear, J. Neurophysiol. 92 (2004) 1–9.
[23] D. Pare, Y. Smith, Distribution of GABA immunoreactivity in the amygdaloid complex of the cat, Neuroscience 57 (1993) 1061–1076.
[24] D. Pare, Y. Smith, The intercalated cell masses project to the central and medial nuclei of the amygdala in cats, Neuroscience 57 (1993) 1077–1090.
[25] D. Plenz, A. Aertsen, Current source density profiles of optical recording maps: a new approach to the analysis of spatio-temporal neural activity patterns, Eur. J. Neurosci. 5 (1993) 437–448.
[26] D.G. Rainnie, E.K. Asprodini, P. Shinnick-Gallagher, Inhibitory transmission in the basolateral amygdala, J. Neurophysiol. 66 (1991) 999–1009.
[27] S. Royer, M. Martina, D. Pare, An inhibitory interface gates impulse traffic between the input and output stations of the amygdala, J. Neurosci. 19 (1999) 10575–10583.
[28] S. Royer, M. Martina, D. Pare, Polarized synaptic interactions between intercalated neurons of the amygdala, J. Neurophysiol. 83 (2000) 3509–3518.
[29] Y. Sekino, K. Obata, M. Tanifuji, M. Mizuno, J. Murayama, Delayed signal propagation via CA2 in rat hippocampal slices revealed by optical recording, J. Neurophysiol. 78 (1997) 1662–1668.
[30] Y. Silberman, L. Shi, J.K. Brunso-Bechtold, J.L. Weiner, Distinct mechanisms of ethanol potentiation of local and paracapsular GABAergic synapses in the rat basolateral amygdala, J. Pharmacol. Exp. Ther. 324 (2008) 251–260.
[31] C. Szinyei, T. Heinbockel, J. Montagne, H.C. Pape, Putative cortical and thalamic inputs elicit convergent excitation in a population of GABAergic interneurons of the lateral amygdala, J. Neurosci. 20 (2000) 8909–8915.
[32] T. Tominaga, Y. Tominaga, H. Yamada, G. Matsumoto, M. Ichikawa, Quantification of optical signals with electrophysiological signals in neural activities of Di-4-ANEPPS stained rat hippocampal slices, J. Neurosci. Methods 102 (2000) 11–23.
[33] Y. Tominaga, M. Ichikawa, T. Tominaga, Membrane potential response profiles of CA1 pyramidal cells probed with voltage-sensitive dye optical imaging in rat hippocampal slices reveal the impact of GABA(A)-mediated feed-forward inhibition in signal propagation, Neurosci. Res. 64 (2009) 152–161.
[34] S. Tsuda, M.Z. Kee, C. Cunha, J. Kim, P. Yan, L.M. Loew, G.J. Augustine, Probing the function of neuronal populations: combining micromirror-based optogenetic photostimulation with voltage-sensitive dye imaging, Neurosci. Res. 75 (2013) 76–81.
[35] C. Wang, M.H. Kang-Park, W.A. Wilson, S.D. Moore, Properties of the pathways from the lateral amygdal nucleus to basolateral nucleus and amygdalostriatal transition area, J. Neurophysiol. 87 (2002) 2593–2601.
[36] C. Wang, W.A. Wilson, S.D. Moore, Role of NMDA, non-NMDA, and GABA receptors in signal propagation in the amygdala formation, J. Neurophysiol. 86 (2001) 1422–1429.
[37] A.R. Woodruff, H. Monyer, P. Sah, GABAergic excitation in the basolateral amygdala, J. Neurosci. 26 (2006) 11881–11887.
[38] A.R. Woodruff, P. Sah, Networks of parvalbumin-positive interneurons in the basolateral amygdala, J. Neurosci. 27 (2007) 553–563.

OPEN ACCESS Freely available online

PLOS ONE

Myosin II ATPase Activity Mediates the Long-Term Potentiation-Induced Exodus of Stable F-Actin Bound by Drebrin A from Dendritic Spines

Toshiyuki Mizui[1,3], Yuko Sekino[1,2*¤a], Hiroyuki Yamazaki[1], Yuta Ishizuka[1], Hideto Takahashi[1¤b], Nobuhiko Kojima[1], Masami Kojima[2,3], Tomoaki Shirao[1*]

1 Department of Neurobiology and Behavior, Gunma University Graduate School of Medicine, Maebashi, Gunma, Japan, **2** Core Research for Evolution Science and Technology, Japan Science and Technology Corporation, Kawaguchi, Saitama, Japan, **3** Bio-interface Research Group, Health Research Institute, National Institute of Advanced Industrial Science and Technology (AIST), Ikeda, Osaka, Japan

Abstract

The neuronal actin-binding protein drebrin A forms a stable structure with F-actin in dendritic spines. NMDA receptor activation causes an exodus of F-actin bound by drebrin A (DA-actin) from dendritic spines, suggesting a pivotal role for DA-actin exodus in synaptic plasticity. We quantitatively assessed the extent of DA-actin localization to spines using the spine-dendrite ratio of drebrin A in cultured hippocampal neurons, and found that (1) chemical long-term potentiation (LTP) stimulation induces rapid DA-actin exodus and subsequent DA-actin re-entry in dendritic spines, (2) Ca^{2+} influx through NMDA receptors regulates the exodus and the basal accumulation of DA-actin, and (3) the DA-actin exodus is blocked by myosin II ATPase inhibitor, but is not blocked by myosin light chain kinase (MLCK) or Rho-associated kinase (ROCK) inhibitors. These results indicate that myosin II mediates the interaction between NMDA receptor activation and DA-actin exodus in LTP induction. Furthermore, myosin II seems to be activated by a rapid actin-linked mechanism rather than slow MLC phosphorylation. Thus the myosin-II mediated DA-actin exodus might be an initial event in LTP induction, triggering actin polymerization and spine enlargement.

Citation: Mizui T, Sekino Y, Yamazaki H, Ishizuka Y, Takahashi H, et al. (2014) Myosin II ATPase Activity Mediates the Long-Term Potentiation-Induced Exodus of Stable F-Actin Bound by Drebrin A from Dendritic Spines. PLoS ONE 9(1): e85367. doi:10.1371/journal.pone.0085367

Editor: Makoto Sato, Osaka University Graduate School of Medicine, Japan

Received September 30, 2013; **Accepted** November 25, 2013; **Published** January 22, 2014

Funding: This work was supported by Grants-in-Aid for Scientific Research (16300117, 19200029) and on Priority Areas - Elucidation of neural network function in the brain - from the Ministry of Education, Culture, Sports, Science and Technology of Japan (20021002). The funders had no role in study design, data collection and analysis, decision to publish, or preparation of the manuscript.

Competing Interests: The authors have declared that no competing interests exist.

* E-mail: yukos@nihs.go.jp (YS); tshirao@ gunma-u.ac.jp (TS)

¤a Current address: Division of Pharmacology, National Institute of Health Sciences, Setagaya-ku, Tokyo, Japan
¤b Current address: Institut de recherches cliniques de Montréal (IRCM), Université de Montréal (UdeM), Québec, Canada

Introduction

Drebrin A is a neuron-specific actin-binding protein that is located at the base of dendritic spine heads [1–3]. Drebrin A binding modifies the pitch of actin filaments [4–5] and forms stable F-actin that is resistant to depolymerization by cytochalasin D [6–7]. Mikati *et al* [8] have recently shown that F-actin that is bound by drebrin A (DA-actin) is stable, and the depolymerization of DA-actin is suppressed at both ends of the filaments. In developing neurons, DA-actin is not observed in dynamic dendritic filopodia, but is observed in more stable dendritic spines [9]. Furthermore, DA-actin is suitable for the formation of a stable higher-order F-actin structure (DA-actin complex), because drebrin A has two F-actin-binding domains that can act cooperatively to enable interfilament interactions [10]. Together, it is suggested that DA-actin forms stable structures of F-actin at the base of dendritic spine heads.

Dendritic spines at rest contain a dynamic F-actin pool that shows quick treadmilling, and a stable pool that shows slow treadmilling. The dynamic pool is observed at the tip of the spine head, whereas the stable pool is located at the base of the spine head [11]. The aforementioned stability and localization of DA-actin suggest that DA-actin is a major component of the stable F-actin pool in dendritic spines, whereas F-actin that is not bound by drebrin A (non-DA-actin) is a major component of the dynamic F-actin pool (for review, see Shirao and González-Billault [12]).

We have previously shown that NMDA receptor activation induces the loss of drebrin A from dendritic spines [13]. Because our previous biochemical analyses revealed that most drebrin A in neurons is bound to F-actin (for a review, see Sekino *et al* [14]), we can extrapolate DA-actin localization from drebrin immunostaining images. Furthermore, fluorescence recovery after photobleaching analysis has demonstrated that drebrin A dynamics in spines are far slower than those of monomeric proteins such as monomeric actin [15] and cortactin [16], indicating that drebrin A remains bound to F-actin even when drebrin A dynamically changes its localization [17]. Together, it is suggested that NMDA receptor activation induces the DA-actin exodus from dendritic spines. However, the mechanism by which NMDA receptor activation links to the DA-actin exodus remains to be elucidated.

It has recently been reported that myosin II ATPase activity is necessary for actin reorganization during long-term potentiation (LTP) induction [18]. We have previously shown that myosin II is

contained in the DA-actin complex [19], but the interaction between myosin II and DA-actin is suppressed in the DA-actin complex [20]. The release of the actomyosin interaction leads to the activation of myosin II ATPase, resulting in reorganization of the actin cytoskeleton through severing of F-actin [21]. Therefore, LTP stimulation might disinhibit the suppressed actomyosin interaction, resulting in the activation of myosin II ATPase.

In this study, we quantitatively assessed the extent to which DA-actin localizes to dendritic spines, clarified DA-actin migration in the context of synaptic plasticity and examined whether myosin II mediates the interaction between NMDA receptor activation and DA-actin exodus.

Materials and Methods

All animal experiments were performed with the permission of the Animal Care and Experimentation Committee, Gunma University, Showa Campus (Maebashi, Japan). All efforts were made to minimize animal suffering and reduce the number of animals used in this study.

Reagents

4-aminopyridine (4-AP) and pyruvate were purchased from Sigma (St. Louis, MO, USA). Hexahydro-1-[(5-iodo-1-naphthalenyl) sulfonyl]-1*H*-1,4-diazepine hydrochloride (ML-7) and (*S*)-(+)-2-Methyl-1-[(4-methyl-5-isoquinolinyl)sulfonyl]-hexahydro-1*H*-1,4-diazepine dihydrochloride (H-1152) were purchased from Calbiochem (San Diego, CA, USA). Ethyleneglycol-*bis* (β-aminoethyl)-N,N,N',N'-tetraacetic acid (EGTA) was purchased from Dojin (Kumamoto, Japan). Tetrodotoxin (TTX) was purchased from Wako (Osaka, Japan). D-(−)-2-amino-5-phosphonopentanoic acid (APV), bicuculline, (S)-(−)-blebbistatin, (R)-(+)-blebbistatin, thapsigargin and nifedipine were purchased from Tocris (Ellisville, MO, USA).

Hippocampal neuron cultures

Timed pregnant Wistar rats (Charles River Laboratories Inc., Yokohama, Japan) were deeply anesthetized with diethyl ether and sacrificed by decapitation. Hippocampi were dissected from the fetuses at embryonic day 18. The hippocampal cells were prepared by trypsinization and mechanical dissociation according to previously described methods [9]. Briefly, the cell suspensions were plated at a density of 5000 cells/cm^2 on coverslips coated with poly-L-lysine (Sigma). Cells were incubated in Minimum Essential Medium (MEM; Invitrogen, San Diego, CA, USA) supplemented with 10% fetal bovine serum (Invitrogen), 0.6% glucose (Wako), and 1 mM pyruvate (Sigma). After the cells achieved attachment, the coverslips were transferred to a culture dish containing a glial monolayer and maintained in normal medium consisting of serum-free MEM, 2% B27 supplement (Invitrogen), 0.6% glucose, and 1 mM sodium pyruvate at 35.8°C in a humidified incubator with 5% CO_2 for 21 days *in vitro* (DIV). Cytosine β-D-arabinofuranoside (10 μM; Sigma) was added to the cultures at 4 DIV to inhibit glial proliferation.

Pharmacological treatments

The chemical LTP (cLTP) stimulation solution used in this study was Mg^{2+}-free Tyrode's solution supplemented with 200 μM glycine, 20 μM bicuculline, 1 μM strychnine and 0.5 μM TTX [22]. For cLTP induction, the neurons were preincubated in cLTP stimulation solution without 200 μM glycine for 20 min, and then stimulated with glycine for the indicated amount of time.

For blocker experiments, the neurons were preincubated in medium supplemented with blocker for 30 min and then stimulated with cLTP stimulation solution or 100 μM glutamate in the presence of each blocker for the indicated amount of time. For the stimulation studies with 90 mM potassium chloride, the neurons were preincubated in Tyrode's solution (119 mM NaCl, 2.5 mM KCl, 2 mM $CaCl_2$, 2 mM $MgSO_4$, 25 mM HEPES [pH 7.4], and 30 mM glucose).

Immunocytochemistry

After three weeks *in vitro*, cells were fixed in 4% paraformaldehyde with 0.1% glutaraldehyde in phosphate-buffered saline (PBS; pH 7.4) at 4°C for 10 min. The fixed cells were permeabilized with 0.1% Triton X-100 in PBS for 3 min and then incubated in blocking solution (3% bovine serum albumin in PBS) for 1 h, followed by an overnight incubation with primary antibodies at 4°C. A monoclonal antibody against drebrin (clone M2F6, hybridoma supernatant [23]) was used at a 1:1 dilution. F-actin was detected with rhodamine-conjugated phalloidin (Molecular Probes, Eugene, OR, USA). After being washed with PBS for 30 min, the cells were incubated for 1 h at room temperature with secondary antibodies. Anti-mouse IgG antibodies conjugated to fluorescein (Cappel, West Chester, PA, USA) were used to detect the monoclonal antibodies against drebrin. After being washed with PBS, the cells were mounted on glass slides with Perma Fluor mounting medium (Thermo Shandon, Pittsburgh, PA, USA).

Labeling of surface GluR1 was performed according to previous reports [22,24] with minor modifications. Briefly, after the cLTP stimulation, surface GluR1 was labeled in live neurons by 30 min incubation with a rabbit polyclonal antibody against the N-terminus of the GluR1 subunit (PC246, 1:15 dilution in glial conditioned media; Calbiochem). After washout of the antibody with Hank's balanced salt solution, the neurons were fixed in 2% PFA for 20 min at 4°C without permeabilization. The surface receptors were visualized using a fluorescein-conjugated goat anti-rabbit secondary antibody (Cappel).

Fluorescence microscopy

All fluorescence images were obtained on a Zeiss Axioplan 2 microscope (Zeiss, Jena, Germany) equipped with a Cool Snap fx CCD camera (Photometrics, Tucson, AZ, USA), a 63×, 1.4 numerical aperture objective lens (Zeiss), and MetaMorph software (Universal Imaging, West Chester, PA, USA). A filter set (86000 Sedat Quad; Chroma, Brattleboro, VT, USA) was mounted in the excitation and emission filter wheels (Ludl Electronic Products, Hawthorne, NY, USA) of the microscope. All data were collected at 1300×1030 resolution at 12 bits/pixel. A single pixel in the image corresponded to a 106 nm^2 area in the specimen plane. The images used for comparison in this study were collected under identical conditions. The captured fluorescence images were analyzed using the MetaMorph program. The GFP, rhodamine, and Cy5 signals were obtained through filters for FITC, Cy3, and Cy5, respectively. We found no fluorescence leakage of these signals through the other filters. The images presented in this study were prepared using Adobe Photoshop software (Adobe Systems, San Jose, CA, USA).

Plasmids and Transfection

Construction of the green fluorescent protein-tagged drebrin A (GFP-DA) has been described previously [25]. At 7 DIV, the hippocampal neurons were transfected with plasmids using a calcium phosphate coprecipitation protocol [26]. Two weeks after transfection, the transfected neurons were analyzed using time-lapse imaging.

Time-lapse imaging

Live time-lapse imaging was performed at 35.8°C on a Zeiss inverted microscope stage using a temperature-controlled chamber with continuous perfusion, as described previously [7]. Briefly, the cell cultures were mounted in a chamber containing Mg^{2+}-free Tyrode's solution supplemented with 20 μM bicuculline, 1 μM strychnine and 0.5 μM TTX. The chamber was maintained and perfused with the same solution. The perfusing solution (1 ml/min) was switched between the control and cLTP stimulation medium using a hydraulic two-way valve switch with a dead space of 3.5 ml between the switch and the bath. Thus, the test medium would reach the chamber 210 sec after flipping the switch (data not shown). The time-lapse images were acquired at 10 sec intervals for 20 min using MetaMorph software.

Image analysis and quantification

All quantifications were performed by an observer who was blind to the experimental conditions, and the morphological analysis was performed using the MetaMorph software. Each experiment was repeated at least three times with independent neuronal preparations.

For quantification, spiny neurons with pyramidal morphology were selected from at least three separate cultures. In our hippocampal cultures, we have previously shown that pyramidal neurons are multipolar cells with a large soma and multiple thick dendritic processes [27]. Therefore, we considered that these multipolar cells were hippocampal pyramidal neurons. Although the hippocampal culture also contains a variety of interneurons, they are comparatively few in number and most are morphologically distinguishable in culture [28].

To measure the surface cluster density of GluR1, the number of GluR1 clusters was measured according to previously described methods [24,29] with minor modifications. Briefly, the surface GluR1 signals were thresholded with intensity at two-fold the dendritic background to mark surface clusters of GluR1 using MetaMorph software. The surface clusters were selected using the 'regions' tool and analyzed using the 'integrated morphometry' feature. Next, the length of the analyzed region on a dendrite was measured. The density of surface GluR1 clusters were obtained by dividing the number of surface GluR1 clusters within a selected dendritic region by the length of the dendrite (50–100 μm total dendritic length per neuron).

Calculation of the spine-dendrite ratio

The spine-dendrite ratio (SDR) used in this study was the average fluorescence signal of the molecule of interest in a dendritic spine head divided by the average fluorescence signal of that molecule in the dendritic shaft at the foot of the spine. To measure the SDR, a single dendrite located between the cell soma and the second branch point (30–80 μm total dendritic length per neuron) was selected from each neuron. The dendritic spines and the shaft in the selected region were outlined on the F-actin fluorescence images, and circles (0.26 μm^2) were drawn at dendritic spine heads and at the foot of the spine in a dendritic shaft, using the 'ellipse region' tool of the MetaMorph software (Fig. 1A). Next, the average fluorescence intensity in each circle (calculated from the fluorescence signal intensity values) was measured using the 'region measurements' tool in the MetaMorph software. The number of spines measured were between 25 and 80 per neuron. The average SDR of spines per neuron was then calculated. The drebrin immunostaining and rhodamine-phalloidin signal intensity values were used to calculate the drebrin and F-actin SDRs, respectively.

Statistical analysis

The statistical analysis included a one-way ANOVA followed by a post hoc Scheffe's test. A Student's t test was performed for comparisons between control and drug-treated neurons. All data were presented as mean ± s.e.m. A p value of <0.01 was considered significant. The statistical analysis was performed using Microsoft Excel (Redmond, WA, USA).

Results

Quantitative assessment of DA-actin in dendritic spines

We used the spine-dendrite ratio (SDR) of drebrin immunostaining intensity to monitor the amounts of DA-actin in dendritic spines. We used the SDR of rhodamine-phalloidin staining intensity to assess the amount of total F-actin. The SDR used in this study is the average fluorescence signal of the molecule of interest in a dendritic spine head divided by the average fluorescence signal of that molecule in the dendritic shaft at the foot of the spine (Fig. 1A). The drebrin SDR of control cultured hippocampal neurons at 21 days *in vitro* (DIV) was 1.65 ± 0.03 ($n = 170$ cells), whereas the actin SDR was 1.67 ± 0.02 ($n = 170$ cells; Fig. 1B), demonstrating that both DA-actin and total F-actin accumulate more in the dendritic spines than the parent dendrites.

Chemical LTP stimulation induces a transient DA-actin exodus

Stimulation with chemical LTP (cLTP) solution for 3 min induced a significant increase in the glutamate receptor subunit 1 (GluR1) cluster density 30 min after treatment (Fig. 2). This increase was inhibited with 50 μM 2-amino-5-phosphonopentanoate (APV), an NMDA receptor blocker (Fig. 2). These data are consistent with an earlier study showing facilitated insertion of α-amino-3-hydroxy-5-methyl-4-isoxazolepropionic acid (AMPA) receptors during cLTP [22].

We examined whether cLTP stimulation would induce DA-actin to exit dendritic spines. At 5 min after cLTP stimulation, the intensity of drebrin immunostaining in dendritic spines was weak, but after 30 min the intensity was similar to that in untreated cells (Fig. 3A). Quantitative analysis showed that both drebrin and actin SDRs were significantly lower at 5 min but recovered after 30 min (Fig. 3B).

To analyze the time course of the DA-actin migration, we transfected a GFP-drebrin A-expressing vector into cultured hippocampal neurons and performed time-lapse imaging. The GFP-drebrin A SDR was transiently decreased following cLTP stimulation, similar to that of the native drebrin A (Fig. 3C). The GFP-drebrin A SDR began to decrease immediately after the neurons were exposed to cLTP solution (arrow in Fig. 3D) and then further declined throughout the period of stimulation. When the stimulation medium was switched back to control medium, the SDR began to rise and returned to the control level in 11 min after the completion of cLTP stimulation (Fig. 3D).

cLTP-induced DA-actin exodus is dependent on myosin II activity

Neurons were pretreated with 100 μM (S)-(−)-blebbistatin (aBL, the active form of blebbistatin), a myosin II ATPase blocker, for 30 min [30]. In the presence of aBL, cLTP stimulation did not affect the localization of either drebrin or actin in dendritic spines (photomicrographs in Fig. 4), and failed to decrease the drebrin and actin SDRs ($n = 30$ cells; $p = 0.37$ for drebrin SDR at 5 min, $p = 0.34$ for actin SDR; Student's *t* test; graphs in Fig. 4). This result indicates that myosin II activity is involved in the DA-actin

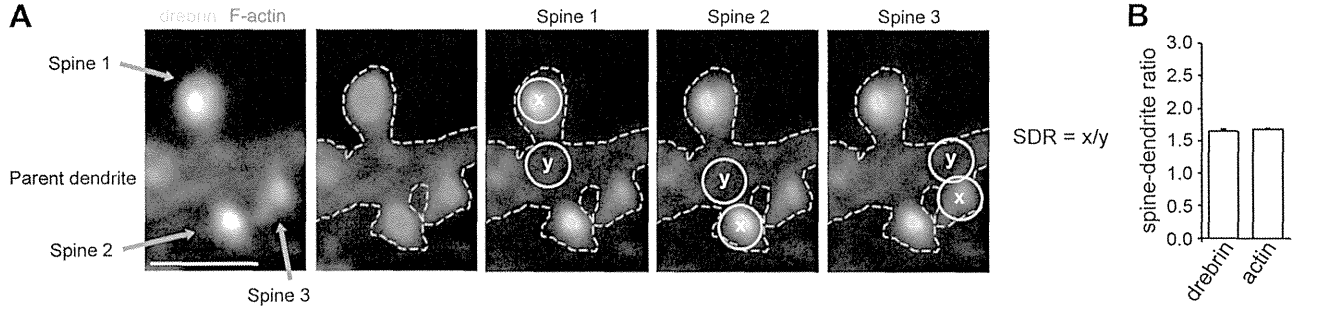

Figure 1. Spine-dendrite ratios of drebrin and actin. (**A**) Fluorescence images of drebrin (green) and F-actin (red) in control hippocampal neurons. The dendritic spines and the parent dendrite in the selected region were outlined on the F-actin fluorescence images (white dotted lines). Scale bar, 2 μm. Circles (0.26 μm^2, yellow) were drawn at the spine head and at the parent dendrite, and the average fluorescence intensities within the circles were measured. The SDR of each spine was obtained by dividing the average intensity of the dendritic spine by that of the parent dendrite. (**B**) The SDR per neuron was obtained as the average SDR of the spines. Bar graph shows the drebrin and actin SDRs of 21-DIV hippocampal neurons (n = 170 cells). Error bars represent s.e.m.
doi:10.1371/journal.pone.0085367.g001

exodus. The inactive form of blebbistatin (iBL) was used as a control. In the presence of iBL, cLTP stimulation significantly decreased the drebrin and actin SDRs.

Various kinds of stimulation induce DA-actin exodus

We stimulated cultured hippocampal neurons with 100 μM glutamate for 10 min, and fixed them immediately after the stimulation. This treatment induced the loss of drebrin and F-actin from dendritic spines (photomicrographs in Fig. 5A). On the other hand, it did not affect the density of spines or presynaptic terminals (Fig. S1). Quantitative analyses showed significant reductions in both the drebrin and actin SDRs (graphs in Fig. 5A).

We then examined whether other kinds of excitatory stimulation affect DA-actin localization. Increased spontaneous firing rates resulting from a 30-minute application of 50 μM bicuculline, a $GABA_A$ receptor blocker, combined with 500 μM 4-aminopyridine, a potassium channel blocker [31], induced a loss of drebrin and F-actin from dendritic spines (photomicrographs in Fig. 5B). A similar decrease was induced by membrane depolarization resulting from a 5-minute application of 90 mM KCl (photomicrographs in Fig. 5C). Quantitative analyses showed that both treatments significantly decreased the drebrin and actin SDRs (graphs in Fig. 5B, C). These data indicate that in addition to cLTP stimulation, various kinds of excitatory stimulation induce a DA-actin exodus.

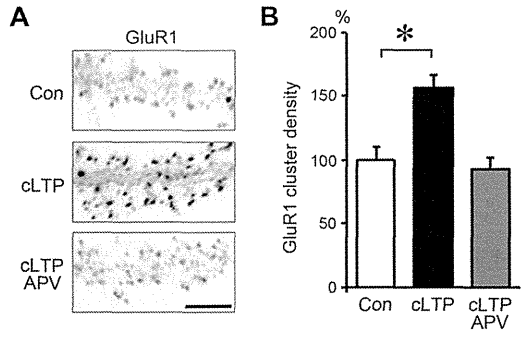

Figure 2. Increase in surface GluR1 immunostaining after chemical LTP (cLTP) stimulation. Neurons (21 DIV) were stimulated with buffer containing 0 μM Mg^{2+}, 200 μM glycine, 20 μM bicuculline, 1 μM strychnine and 0.5 μM TTX (cLTP stimulation) for 3 min. (**A**) Surface GluR1 was labeled before the stimulation (top panel; Con) or 30 min after the stimulation (middle panel; cLTP). Note that cLTP stimulation remarkably increased surface GluR1 immunostaining. The increase was completely blocked by APV (bottom panel; cLTP APV). Scale bar, 7 μm. (**B**) Quantitative analysis of surface GluR1 cluster density along dendrites. Data are expressed as percentages relative to the average of control neurons. In the absence of APV, cLTP stimulation significantly increased the density of surface GluR1 clusters (n = 21 cells; $p<0.01$, Scheffe's test). In contrast, in the presence of APV, no increase in surface GluR1 cluster density was observed following cLTP stimulation (cLTP APV). Error bars represent s.e.m.
doi:10.1371/journal.pone.0085367.g002

Localization of DA-actin and non-DA-actin is differentially regulated by glutamate receptor subtypes

We examined the effect of APV on DA-actin and total F-actin levels in dendritic spines. In the presence of 50 μM APV, drebrin and F-actin were localized at dendritic spines, and this localization was not changed by glutamate stimulation (photomicrographs in Fig. 6A).

However, quantitative analysis showed that the treatment of neurons with APV for 30 min resulted in significant increases in both drebrin and actin SDRs relative to controls. Interestingly, the increase in actin SDR (ca. 130% of control) is smaller than that of the drebrin SDR (ca. 180% of control; Fig. 6A). This indicates that NMDA receptor activity affects the basal accumulation level of DA-actin in dendritic spines more strongly than that of non-DA-actin. If non-DA-actin is not at all affected by APV, the above data suggest that about 40% of total F-actin is DA-actin. Furthermore, in the presence of APV, glutamate stimulation failed to decrease the drebrin SDR but did decrease the actin SDR (Fig. 6A). The disparity between drebrin and actin SDRs indicates that glutamate stimulation decreases the non-DA-actin even in the presence of APV.

Together, it is suggested that the NMDA receptor mediates both the glutamate-induced DA-actin exodus and the basal accumulation of DA-actin in dendritic spines, whereas glutamate receptor subtypes other than the NMDA receptor, such as AMPA or metabotropic glutamate receptors, mediate the non-DA-actin exodus.

The DA-actin exodus is not regulated by voltage-dependent Ca^{2+} channels or intracellular Ca^{2+} stores

Because NMDA receptor activation leads to Ca^{2+} influx, we examined whether Ca^{2+} regulates the DA-actin distribution. When extracellular Ca^{2+} was chelated by 20 mM ethylene glycol tetraacetic acid (EGTA), the localization pattern of drebrin and F-

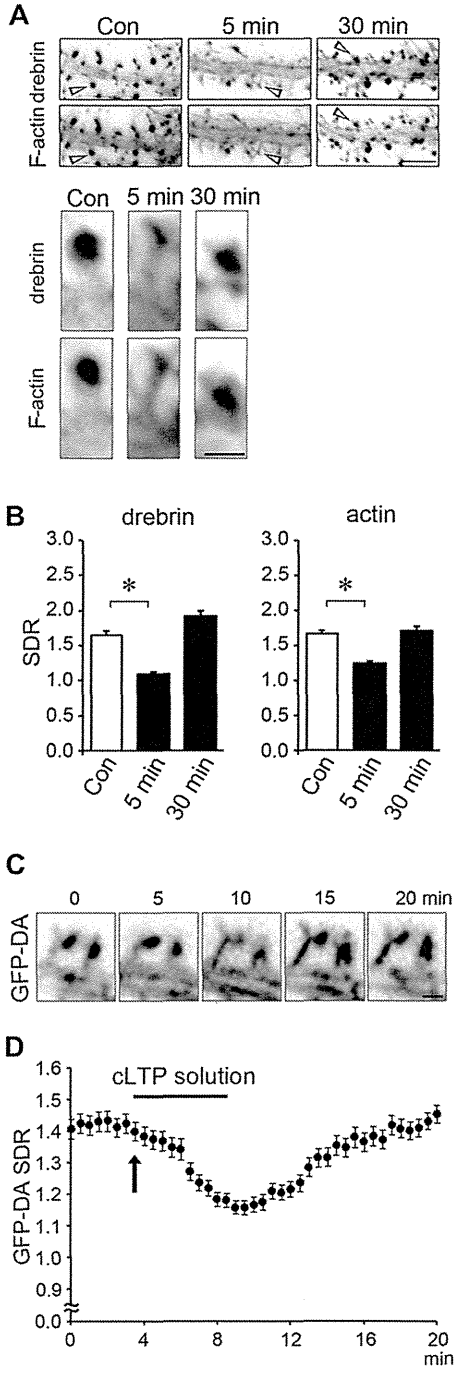

Figure 3. Chemical LTP (cLTP) stimulation induces the exodus and re-entry of DA-actin. (**A**) Neurons (21 DIV) were stimulated with a buffer containing 0 μM Mg^{2+}, 200 μM glycine, 20 μM bicuculline, 1 μM strychnine and 0.5 μM TTX (cLTP stimulation) for 3 min and then fixed 5 or 30 min after stimulation. The fixed cells were double-labeled for drebrin and F-actin. Scale bars, 5 μm and 1 μm in upper and lower panels, respectively. The lower panels show the higher-magnification images of the spines (indicated by arrow heads) in the upper panels. (**B**) Bar graphs represent the spine-dendrite ratios (SDRs) for drebrin and actin. cLTP stimulation significantly decreased the drebrin and actin SDRs at 5 min (n = 30 cells; $p<0.01$, Student's *t* test). Error bars represent s.e.m. (**C, D**) We transfected 7-DIV neurons with a GFP-drebrin A (GFP-DA)-expressing vector and performed time-lapse imaging at 21 DIV. Scale bar, 1 μm. (C) shows the GFP-DA images at 0, 5, 10, 15 and 20 min after the start of the time-lapse recording. The neurons were stimulated with cLTP solution from 3.5 min (indicated by an arrow) to 8.5 min. In (D), closed circles represent data obtained at 30-sec intervals. Error bars represent s.e.m. (n = 7 neurons). The GFP-DA SDR began to decrease soon after cLTP stimulation. When the stimulation was stopped, the GFP-DA SDR began to increase and recovered to control levels within 10 min.
doi:10.1371/journal.pone.0085367.g003

actin in dendritic spines was similar for both with and without glutamate stimulation (photomicrographs in Fig. 6B). However, quantitative analysis showed that EGTA treatment significantly increased both the drebrin and actin SDRs compared with control neurons. Following the extracellular Ca^{2+} chelation, glutamate stimulation failed to induce decreases in drebrin and actin SDRs (n = 30 cells; p = 0.88 for drebrin SDR, p = 0.84 for actin SDR; Student's *t* test; graphs in Fig. 6B). These data indicate that Ca^{2+} influx is involved in the changes in both DA-actin and non-DA-actin distribution.

Inhibition of L-type voltage-dependent Ca^{2+} channels with 20 μM nifedipine did not block glutamate-induced changes in drebrin and F-actin localization (photomicrographs in Fig. 6C). Quantitative analysis also showed that nifedipine treatment did not inhibit the glutamate-induced decreases in drebrin and actin SDRs. However, in the absence of glutamate stimulation, nifedipine treatment significantly increased the drebrin and actin SDR levels, similar to the results obtained with APV and EGTA treatments (graphs in Fig. 6C). This indicates that voltage-dependent Ca^{2+} channels regulate the accumulation of DA-actin in dendritic spines, but do not regulate the DA-actin exodus. However, we cannot exclude the possibility that the increase of the basal SDR is due to inhibition of voltage-dependent Ca^{2+} channels in the presynaptic terminus.

Inhibition of Ca^{2+} release from intracellular stores with 1 μM thapsigargin [32] did not block glutamate-induced changes in drebrin and F-actin localization (photomicrographs in Fig. 6D). Quantitative analysis showed that thapsigargin neither increased the drebrin and actin SDRs (n = 30 cells; p = 0.99 for drebrin SDR, p = 0.50 for actin SDR; Student's *t* test) nor blocked the glutamate-induced decreases in drebrin and actin SDRs (n = 30 cells: $p<0.01$, Scheffe's test; graphs in Fig. 6D).

Together, these data indicate that DA-actin exodus is regulated by NMDA receptors, but not by voltage-dependent Ca^{2+} channels. On the other hand, the basal accumulation of DA-actin in dendritic spines is regulated by both NMDA receptors and voltage-dependent Ca^{2+} channels. Ca^{2+} release from intracellular stores is not involved in either the DA-actin exodus or the basal accumulation of DA-actin.

Glutamate-induced DA-actin exodus is also dependent on myosin II ATPase activity

We examined whether myosin II ATPase is involved in the glutamate-induced DA-actin exodus. In the presence of aBL, drebrin localization at dendritic spines was not affected by glutamate stimulation (photomicrographs in Fig. 7), and glutamate stimulation did not induce a decrease in drebrin SDR (n = 30 cells; p = 0.06, Student's *t* test; graph in Fig. 7). Interestingly, the actin SDR was slightly, but significantly, decreased upon glutamate stimulation (graph in Fig. 7), although the decrease was not remarkable compared with that in the presence of iBL (Fig. 7). This result indicates that inhibition of myosin II ATPase does not completely block the exodus of F-actin, indicating that a small amount of F-actin other than DA-actin exits dendritic spines in response to glutamate stimulation.

Together, it is indicated that the glutamate-induced as well as the cLTP-induced DA-actin exodus depends on myosin II ATPase, but the glutamate-induced non-DA-actin exodus is at

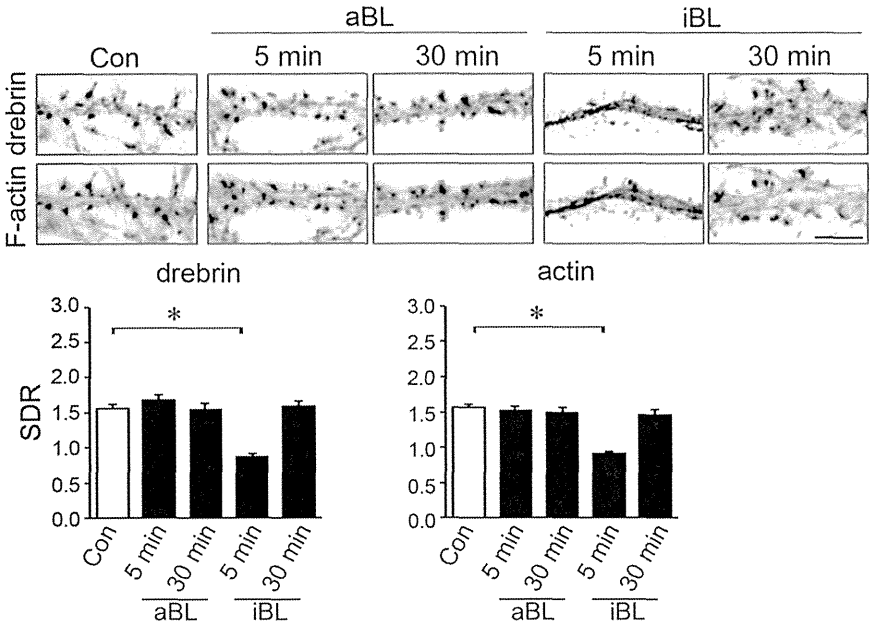

Figure 4. cLTP-induced DA-actin exodus is blocked by an inhibitor of myosin II ATPase. Neurons (21 DIV) were preincubated with 100 μM (S)-(−)-blebbistatin (aBL, the active form of blebbistatin) for 30 min and then stimulated with cLTP solution for 3 min. (R)-(+)-blebbistatin (iBL, the inactive form of blebbistatin) was used as a control. Scale bars, 5 μm. F-actin images indicate that spines kept their structure during the experiment although their shapes were changed. The aBL-treated neurons did not show a decrease in the drebrin and actin SDRs at either 5 min or 30 min after cLTP stimulation (n = 30 cells; Student's test), whereas iBL-treated neurons showed a significant decrease in the drebrin and actin SDRs at 5 min (n = 30 cells; $p<0.01$, Scheffe's test), similar to that observed in control neurons in Fig. 3. Error bars represent s.e.m.
doi:10.1371/journal.pone.0085367.g004

least partly independent of myosin II ATPase. This myosin II-independent loss of non-DA-actin might correspond to the NMDA receptor-independent loss of non-DA-actin shown in Fig. 6A.

The DA-actin exodus is not dependent on phosphorylation of myosin light chain

To examine whether the phosphorylation of myosin light chain (MLC) is involved in the DA-actin exodus, we inhibited myosin

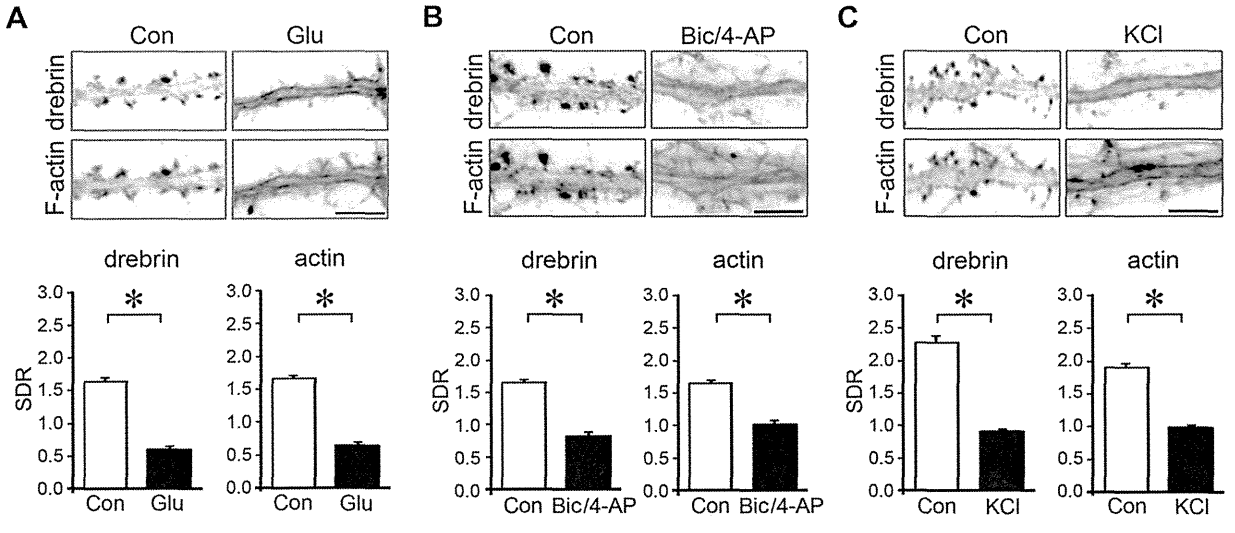

Figure 5. Effects of various excitatory stimulations on DA-actin distribution. Images were obtained from neurons (21 DIV) double-labeled for drebrin and F-actin. Bar graphs represent the spine-dendrite ratios (SDRs) for drebrin and actin. (**A–C**) Neurons were stimulated with 100 μM glutamate for 10 min (A), 50 μM bicuculline and 500 μM 4-aminopyridine (Bic/4-AP) for 10 min (B), or 90 mM KCl in Tyrode's solution for 5 min (C). F-actin images indicate that spines kept their structure during the experiment although their shapes were changed. After stimulation, the drebrin and F-actin clusters in the spines disappeared, and a linear staining pattern appeared along the dendrite. Both the drebrin and actin SDRs were significantly decreased (glutamate, n = 170 cells; Bic/4-AP, n = 30 cells; KCl, n = 30 cells; $p<0.01$, Student's *t* test). Note that the control drebrin and actin SDRs in (C) were greater than the other SDRs because Tyrode's solution was used instead of normal medium. Scale bars, 5 μm. Error bars represent s.e.m.
doi:10.1371/journal.pone.0085367.g005

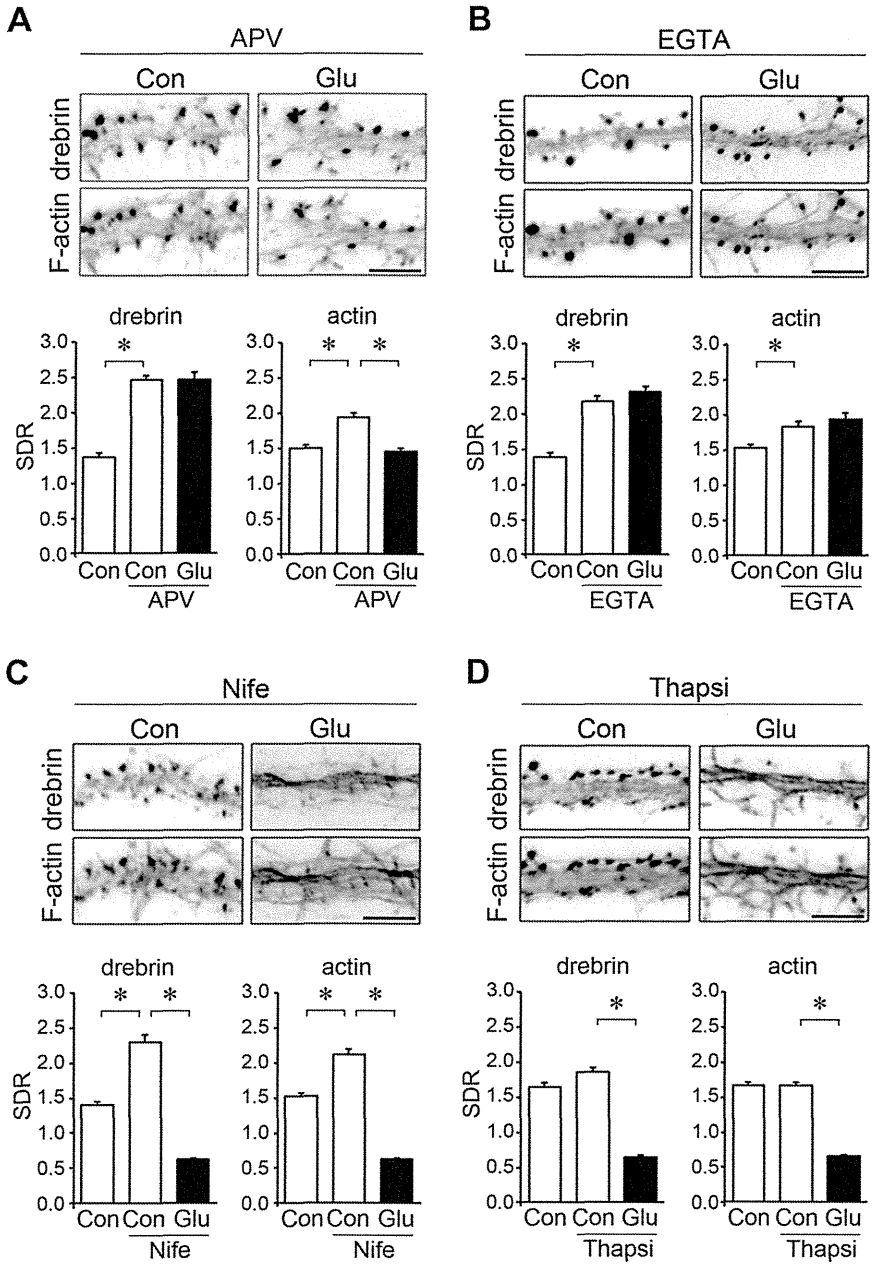

Figure 6. Effects of various inhibitors of Ca^{2+} entry on DA-actin distribution. Neurons (21 DIV) were incubated in normal medium containing 50 μM APV (A), 20 mM EGTA (B), 20 μM nifedipine (C), or 1 μM thapsigargin (D) for 30 min. The neurons were then stimulated with 100 μM glutamate for an additional 10 min. F-actin images indicate that spines kept their structure during the experiment although their shapes were changed. Scale bars, 5 μm. (**A**) APV pretreatment significantly increased both the drebrin and actin SDRs (n = 30 cells; $p<0.01$, Scheffe's test). In the presence of APV, glutamate stimulation significantly decreased the actin SDR (n = 30 cells; $p<0.01$, Student's *t* test) but not the drebrin SDR (n = 30 cells; $p = 0.52$, Student's *t* test). (**B**) EGTA significantly increased the drebrin and actin SDRs (n = 30 cells; $p<0.01$, Scheffe's test), and blocked the glutamate-induced decreases in drebrin and actin SDRs (n = 30 cells; Student's *t* test). (**C**) Nifedipine significantly increased the drebrin and actin SDRs (n = 30; $p<0.01$, Scheffe's test), but did not block the glutamate-induced decrease in drebrin and actin SDRs (n = 30; $p<0.01$, Scheffe's test). (**D**) Thapsigargin neither increased the drebrin and actin SDRs (n = 30; Student's *t* test) nor blocked the glutamate-induced decreases in drebrin and actin SDRs (n = 30; $p<0.01$, Scheffe's test). Error bars represent s.e.m.
doi:10.1371/journal.pone.0085367.g006

light chain kinase (MLCK). When MLCK activity was inhibited with 10 μM ML-7, glutamate stimulation induced the loss of drebrin and F-actin from dendritic spines (photomicrographs in Fig. 8A). Quantitative analysis showed that the ML-7 treatment did not change the drebrin and actin SDR levels compared with control neurons, and did not inhibit the glutamate-induced decreases in the drebrin and actin SDRs (Fig. 8A).

We then inhibited ROCK activity with 1 μM H-1152. In the presence of H-1152, glutamate stimulation induced the loss of drebrin and F-actin from dendritic spines (photomicrographs in Fig. 8B). Quantitative analysis showed that the H-1152 treatment did not change the drebrin and actin SDR levels compared with control neurons, and did not inhibit the glutamate-induced decreases in the drebrin and actin SDRs (Fig. 8B).

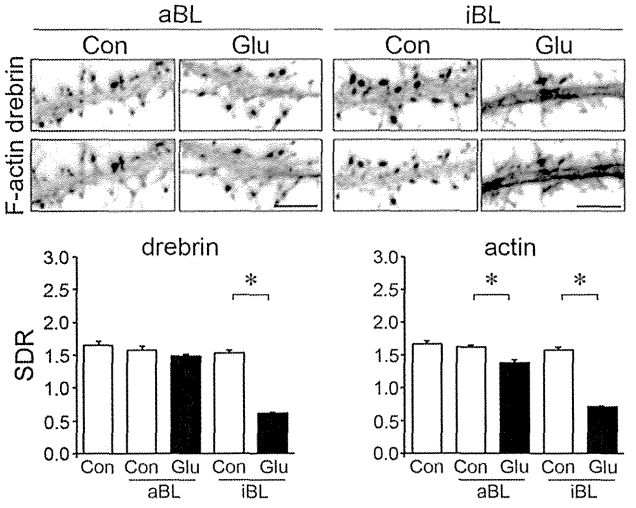

Figure 7. Glutamate-induced DA-actin exodus is blocked by an inhibitor of myosin II ATPase. Neurons (21 DIV) were preincubated with 100 μM aBL for 30 min and then stimulated with 100 μM glutamate for 10 min. F-actin images indicate that spines kept their structure during the experiment although their shapes were changed. Scale bars, 5 μm. The drebrin SDR of aBL-treated neurons was not decreased by glutamate stimulation (n = 30 cells; p = 0.06, Student's *t* test), although that of iBL-treated neurons was decreased (n = 30 cells: p<0.01, Scheffe's test). On the other hand, the actin SDR of aBL-pretreated neurons was slightly, but significantly, decreased by glutamate stimulation (n = 30 cells; p<0.01, Scheffe's test), although the reduction was much smaller than that observed in iBL-pretreated neurons (n = 30 cells; p<0.01, Student's *t* test). Error bars represent s.e.m.
doi:10.1371/journal.pone.0085367.g007

Because MLCK and ROCK phosphorylate MLC [33], the above data suggest that MLC phosphorylation is not involved in the DA-actin exodus.

Discussion

In the present study we demonstrated that (1) chemical long-term potentiation (cLTP) stimulation induces rapid DA-actin exodus and subsequent DA-actin re-entry in dendritic spines, (2) Ca^{2+} influx through NMDA receptors regulates both the exodus and the basal accumulation of DA-actin, and (3) the DA-actin exodus is blocked by a myosin II ATPase inhibitor, but is not blocked by either MLCK or ROCK inhibitors.

These results indicate that Ca^{2+} influx through NMDA receptors induces the DA-actin exodus in LTP induction, and that myosin II mediates the interaction between NMDA receptor activation and DA-actin exodus (Fig. S2). Furthermore, the Ca^{2+} influx seems to activate myosin II ATPase by a rapid actin-linked mechanism instead of slow MLC phosphorylation. Thus the myosin II-mediated DA-actin exodus might be an initial event in LTP induction, triggering actin polymerization and spine enlargement.

SDR analysis of DA-actin migration in and out of dendritic spines

In the present study, using drebrin SDR, we found that APV treatment not only inhibits the DA-actin exodus but also facilitates the accumulation of DA-actin in dendritic spines. In our previous studies, we could not detect any facilitative effect of APV treatment on drebrin accumulation in dendritic spines, because we used drebrin cluster density along dendrites for assessing the dynamic changes in drebrin localization [13,17]. Although this method is sensitive enough to detect the loss of drebrin from

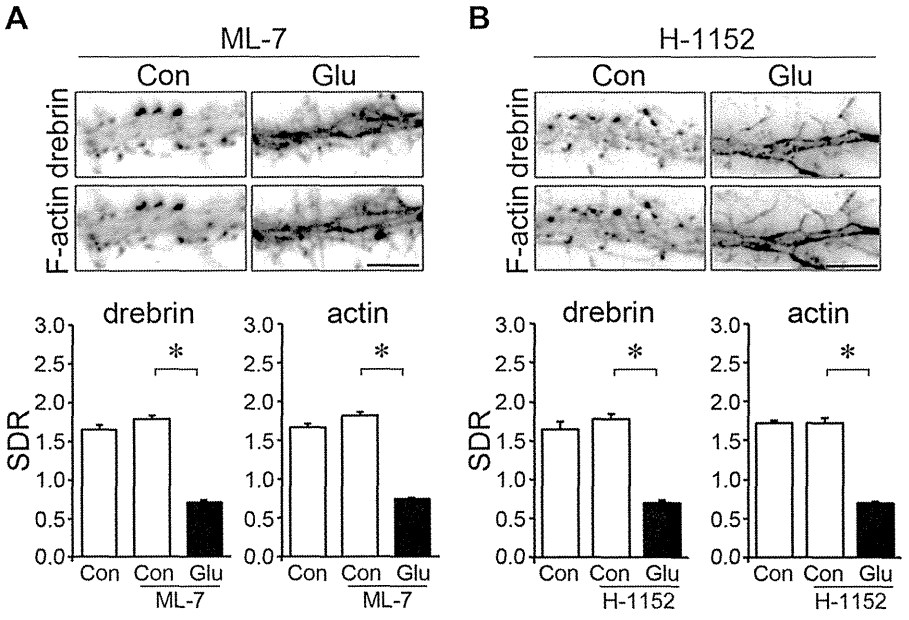

Figure 8. The DA-actin exodus is not blocked by inhibitors of myosin light chain kinase (MLCK) or Rho-associated kinase (ROCK). Neurons (21 DIV) were preincubated with 10 μM of ML-7, an inhibitor of MLCK (A) or 1 μM H-1152, an inhibitor of ROCK (B) for 30 min, and then stimulated with 100 μM glutamate for 10 min. Neither ML-7 (n = 30 cells; drebrin SDR p<0.01, actin SDR p<0.01, Scheffe's test) nor H1152 (n = 30 cells; drebrin SDR p<0.01, actin SDR p<0.01, Scheffe's test) blocked the DA-actin exodus. F-actin images indicate that spines kept their structure during the experiment although their shapes were changed. Scale bars, 5 μm.
doi:10.1371/journal.pone.0085367.g008

dendritic spines, it is not sensitive enough to detect the accumulation of drebrin in dendritic spines.

By comparing the changes in drebrin and actin SDRs we can extrapolate the changes in non-DA-actin, because the total F-actin shown by the actin SDR consists of DA-actin and non-DA-actin. In the present study we found that the glutamate-induced exoduses of DA-actin and non-DA-actin are differentially regulated by each glutamate receptor subtype. Thus measurement of SDR is a useful method to analyze the migration of proteins in and out of dendritic spines.

The DA-actin exodus may trigger the facilitation of F-actin polymerization in dendritic spines

After NMDA receptor activation in LTP induction, facilitation of actin polymerization and spine enlargement are observed [34–35]. However, the underlying mechanisms of these processes have not been elucidated. The present study shows that the total amount of F-actin in dendritic spines transiently decreases shortly after cLTP stimulation, resulting from a DA-actin exodus. Once the total F-actin in dendritic spines reduces by the DA-actin exodus, monomeric actin is likely to immediately refill the vacant space by diffusion [15]. The increase in the amount of monomeric actin is known to facilitate F-actin polymerization [36]. In addition, the treadmilling rate of DA-actin is low [8], suggesting that the high level of DA-actin in dendritic spines makes the average treadmilling rate of total F-actin lower in resting dendritic spines. Because quickly-treadmilling non-DA-actin predominates in dendritic spines after the DA-actin exodus, the average treadmilling rate of total F-actin is increased. Together, it is indicated that the DA-actin exodus increases the monomeric actin content and the treadmilling rate of F-actin in dendritic spines, resulting in the facilitation of F-actin polymerization and spine enlargement (Fig. S2).

Possible molecular mechanism for how Ca^{2+} influx activates myosin II ATPase in dendritic spines

Myosin II ATPase is known to be activated by MLC phosphorylation or by an actin-linked mechanism. The important issue remaining is which molecular mechanism is related to the DA-actin exodus. MLCK and ROCK are two major candidates for the regulator of MLC phosphorylation [33]. The present study reveals that block of neither MLCK nor ROCK inhibits the DA-actin exodus. This finding suggests that MLC phosphorylation is not involved in the DA-actin exodus.

Thus activation of myosin II ATPase by an actin-linked mechanism is likely involved in the DA-actin exodus. In the actin-linked mechanism, myosin II ATPase is activated by the release of the suppressed actomyosin interaction. In mammalian skeletal muscles, when Ca^{2+} binds to the troponin complex, the actomyosin interaction suppressed by tropomyosin is released, and consequently myosin II ATPase is activated. Because drebrin A inhibits the myosin II ATPase activity similar to tropomyosin [20], drebrin A is thought to be the counterpart of tropomyosin in dendritic spines [14]. Therefore it is suggested that drebrin A protects actin filaments from the interaction with myosin II in the resting dendritic spines, resulting in the inhibition of myosin II ATPase. Once NMDA receptors are activated, the Ca^{2+} influx through NMDA receptors may change the location of drebrin A on the actin filaments, releasing the actomyosin interaction suppressed by drebrin A. Consequently myosin II ATPase is activated in dendritic spines. Thus myosin II ATPase activation by an actin-linked mechanism may be an underlying molecular mechanism for the DA-actin exodus.

Furthermore, the present data shows that the DA-actin exodus occurs immediately after cLTP stimulation. The activation of myosin II ATPase by an actin-linked mechanism occurs within 20 ms after stimulation [37]. Thus the myosin-II mediated DA-actin exodus might be an initial event in LTP induction, triggering actin polymerization and spine enlargement.

Role of DA-actin re-entry into dendritic spines

DA-actin re-entry follows the DA-actin exodus. In the present study we found that the LTP-induced DA-actin exodus triggers F-actin polymerization and spine enlargement. The DA-actin re-entry may be related to maintenance of LTP. After the DA-actin re-entry, the dynamic and stable F-actin pools are probably reestablished in the dendritic spines. As a result, polymerization and depolymerization of F-actin is balanced in dendritic spines and the enlarged spine morphology is maintained (Fig. S2). In fact, long lasting increases in F-actin and drebrin content in dendritic spines have been reported when LTP is maintained *in vivo* [38].

What are the underlying mechanisms of DA-actin re-entry? Reduction of the Ca^{2+} influx into dendritic spines might induce the DA-actin re-entry, because the basal accumulation of DA-actin is negatively regulated by Ca^{2+} influx through NMDA receptors and voltage-dependent Ca^{2+} channels in resting spines. Another possible mechanism is a signaling cascade linked to AMPA receptors. LTP stimulation is known to increase the AMPA receptor density in dendritic spines [39]. Because AMPA receptor activity facilitates accumulation of DA-actin in the dendritic spines of immature neurons [17], AMPA receptors might also be involved in the DA-actin re-entry in mature neurons.

Supporting Information

Figure S1 Effects of glutamate stimulation on the density of spines and presynaptic terminals. (**A**) DiI staining of hippocampal neurons. Fixed cultures on coverslips were bathed in PBS and placed on the stage of an inverted phase microscope. Individual cells were stained with 1,1′-dioctadecyl-3,3,3′,3′-tetramethylindocarbocyanine perchlorate (DiI; Molecular Probes, Inc., Eugene, OR). The DiI was dissolved in vegetable oil to saturation, loaded into a glass micropipette (Eppendorf), and applied by pressure ejection onto the multipolar neurons. The coverslips were then placed at room temperature in small petri dishes containing PBS. After 12–24 h, which allowed for sufficient transport of the dye, cells were examined by fluorescence microscopy. The spine morphology of boxed areas in upper panels are shown at higher magnification in middle panels. Note that the spines kept their structures during the experiment. Scale bars, 10 μm. Left panel in the bottom shows the density of dendritic spines. To measure spine density, the number of spines per cell was then counted for 25 cells (50–100 μm total dendritic length per neuron). Significant differences were not observed between the control (n = 42 dendrites) and glutamate-treated dendrites (n = 44 dendrites; p = 0.73, Student's t test). Bar graphs represent dendritic spine density. The cumulative frequency plots in the bottom show distribution of spine length and spine width. The glutamate treatment significantly increased the spine length (control, 1.39±0.03 μm, n = 42 dendrites; glutamate, 1.72±0.05 μm, n = 44 dendrites, $p<0.01$, Student's t test) and reduced the spine width (control, 0.96±0.01 μm, n = 42 dendrites; glutamate, 0.82±0.02 μm, n = 44 dendrites, $p<0.01$, Student's t test). (**B**) Triple-labeled images of drebrin, F-actin and synapsin I in hippocampal neurons. Scale bars, 10 μm. (**C**) Bar graphs represent the density of synapsin I clusters. Synapsin I cluster density was measured according to previously described methods

(Takahashi et al., 2009). No significant differences in the density of synapsin I clusters were detected between control (n = 30 dendrites) and glutamate-stimulated neurons (n = 30 dendrites; p = 0.86, Student's t test). Data are presented as mean ± s.e.m.
(TIF)

Figure S2 Model for architectural changes in the actin cytoskeleton during LTP formation. (**A**) Dendritic spines in the resting state contain a dynamic F-actin pool (non-DA-actin) at the tip of the spine head, and a stable pool (DA-actin) in the base of the spine head. Although the dynamic F-actin pool shows quick treadmilling, polymerization and depolymerization of F-actin is balanced, consequently maintaining spine morphology. (**B**) Once Ca^{2+} enters through NMDA receptors, it activates myosin II ATPase through disinhibition of the DA-actin and myosin-II interaction. Consequently DA-actin exits the dendritic spine head and simultaneously monomeric actin refills the vacant space in the spine head. Both these changes cooperate to facilitate the polymerization of non-DA-actin, which is the predominant component of an enlargement F-actin pool in the spine head. Accordingly the spine head is enlarged. (**C**) Ca^{2+} reduction and/or APMA receptor activation induce DA-actin re-entry. The DA-actin re-entry reconstitutes the dynamic and stable F-actin pools in dendritic spines, contributing to maintenance of the enlarged spine morphology until the next DA-actin exodus is triggered.
(EPS)

Acknowledgments

We thank Drs. Kenji Hanamura and Mitsuyoshi Saito for helpful discussions and Ms. Tomoko Takahashi for technical assistance.

Author Contributions

Conceived and designed the experiments: TM YS TS. Performed the experiments: TM HY YI HT. Analyzed the data: TM YS HY YI HT NK MK. Wrote the paper: TM YS TS.

References

1. Shirao T, Kojima N, Nabeta Y, Obata K (1989) Two forms of drebrins, developmentally regulated brain proteins, in rat. Proc Japan Acad 65: 169–172.
2. Ishikawa R, Hayashi K, Shirao T, Xue Y, Takagi T, et al. (1994) Drebrin, a development-associated brain protein from rat embryo, causes the dissociation of tropomyosin from actin filaments. J Biol Chem 269: 29928–29933.
3. Aoki C, Sekino Y, Hanamura K, Fujisawa S, Mahadomrongkul V, et al. (2005) Drebrin A is a postsynaptic protein that localizes in vivo to the submembranous surface of dendritic sites forming excitatory synapses. J Comp Neurol 483: 383–402.
4. Grintsevich EE, Galkin VE, Orlova A, Ytterberg AJ, Mikati MM, et al. (2010) Mapping of drebrin binding site on F-actin. J Mol Biol 398: 542–554.
5. Sharma S, Grintsevich EE, Phillips ML, Reisler E, Gimzewski JK (2011) Atomic force microscopy reveals drebrin induced remodeling of f-actin with subnanometer resolution. Nano Lett 11: 825–827.
6. Asada H, Uyemura K, Shirao T (1994) Actin-binding protein, drebrin, accumulates in submembranous regions in parallel with neuronal differentiation. J Neurosci Res 38: 149–159.
7. Mizui T, Kojima N, Yamazaki H, Katayama M, Hanamura K, et al. (2009) Drebrin E is involved in the regulation of axonal growth through actin-myosin interactions. J Neurochem 109: 611–622.
8. Mikati MA, Grintsevich EE, Reisler E (2013) Drebrin-induced Stabilization of Actin Filaments. J Biol Chem 288: 19926–19938.
9. Takahashi H, Sekino Y, Tanaka S, Mizui T, Kishi S, et al. (2003) Drebrin-dependent actin clustering in dendritic filopodia governs synaptic targeting of postsynaptic density-95 and dendritic spine morphogenesis. J Neurosci 23: 6586–6595.
10. Worth DC, Daly CN, Geraldo S, Oozeer F, Gordon-Weeks PR (2013) Drebrin contains a cryptic F-actin-bundling activity regulated by Cdk5 phosphorylation. J Cell Biol 202: 793–806.
11. Honkura N, Matsuzaki M, Noguchi J, Ellis-Davies GC, Kasai H (2008) The subspine organization of actin fibers regulates the structure and plasticity of dendritic spines. Neuron 57: 719–729.
12. Shirao T, González-Billault C (2013) Actin filaments and microtubules in dendritic spines. J Neurochem 126: 155–164.
13. Sekino Y, Tanaka S, Hanamura K, Yamazaki H, Sasagawa Y, et al. (2006) Activation of N-methyl-D-aspartate receptor induces a shift of drebrin distribution: Disappearance from dendritic spines and appearance in dendritic shafts. Mol Cell Neurosci 31: 493–504.
14. Sekino Y, Kojima N, Shirao T (2007) Role of actin cytoskeleton in dendritic spine morphogenesis. Neurochem Int 51: 92–104.
15. Star EN, Kwiatkowski DJ, Murthy VN (2002) Rapid turnover of actin in dendritic spines and its regulation by activity. Nat Neurosci 5: 239–246.
16. Iki J, Inoue A, Bito H, Okabe S (2005) Bi-directional regulation of postsynaptic cortactin distribution by BDNF and NMDA receptor activity. Eur J Neurosci 22: 2985–2994.
17. Takahashi H, Yamazaki H, Hanamura K, Sekino Y, Shirao T (2009) AMPA receptor inhibition causes abnormal dendritic spines by destabilizing drebrin. J Cell Sci 122: 1211–1229.
18. Rex CS, Gavin CF, Rubio MD, Kramar EA, Chen LY, et al. (2010) Myosin IIb regulates actin dynamics during synaptic plasticity and memory formation. Neuron 67: 603–617.
19. Cheng XT, Hayashi K, Shirao T (2000) Non-muscle myosin IIB-like immunoreactivity is present at the drebrin-binding cytoskeleton in neurons. Neurosci Res 36: 167–173.
20. Hayashi K, Ishikawa R, Ye LH, He XL, Takata K, et al. (1996) Modulatory role of drebrin on the cytoskeleton within dendritic spines in the rat cerebral cortex. J Neurosci 16: 7161–7170.
21. Murrell MP, Gardel ML (2012) F-actin buckling coordinates contractility and severing in a biomimetic actomyosin cortex. Proc Natl Acad Sci USA 109: 20820–20825.
22. Lu W, Man H, Ju W, Trimble WS, MacDonald JF, et al. (2001) Activation of synaptic NMDA receptors induces membrane insertion of new AMPA receptors and LTP in cultured hippocampal neurons. Neuron 29: 243–254.
23. Shirao T, Obata K (1986) Immunochemical homology of 3 developmentally regulated brain proteins and their developmental change in neuronal distribution. Brain Res 394: 233–244.
24. Swayze RD, Lise MF, Levinson JN, Phillips A, El-Husseini A (2004) Modulation of dopamine mediated phosphorylation of AMPA receptors by PSD-95 and AKAP79/150. Neuropharmacology 47: 764–778.
25. Hayashi K, Shirao T (1999) Change in the shape of dendritic spines caused by overexpression of drebrin in cultured cortical neurons. J Neurosci 19: 3918–3925.
26. Xie H (1984) Differences in the Efficiency and Stability of Gene Expression after Transfection and Nuclear Injection: A Study with a Chick δ-Crystallin Gene. Cell Struct Funct 8: 315–325.
27. Hanamura K, Mizui T, Kakizaki T, Roppongi RT, Yamazaki H, et al. (2010) Low accumulation of drebrin at glutamatergic postsynaptic sites on GABAergic neurons, Neuroscience 169: 1489–1500.
28. Kaech S, Banker G (2006) Culturing hippocampal neurons, Nat Protoc 1: 2406–2415.
29. Xie Z, Srivastava DP, Photowala H, Kai L, Cahill ME, et al. (2007) Kalirin-7 controls activity-dependent structural and functional plasticity of dendritic spines. Neuron 56: 640–656.
30. Ryu J, Liu L, Wong TP, Wu DC, Burette A, et al. (2006) A critical role for myosin IIb in dendritic spine morphology and synaptic function. Neuron 49: 175–182.
31. Hardingham GE, Fukunaga Y, Bading H (2002) Extrasynaptic NMDARs oppose synaptic NMDARs by triggering CREB shut-off and cell death pathways. Nat Neurosci 5: 405–414.
32. Yuste R, Majewska A, Holthoff K (2000) From form to function: calcium compartmentalization in dendritic spines. Nat Neurosci 3: 653–659.
33. Matsumura F (2005) Regulation of myosin II during cytokinesis in higher eukaryotes. Trends Cell Biol 15: 371–377.
34. Matsuzaki M, Honkura N, Ellis-Davies GC, Kasai H (2004) Structural basis of long-term potentiation in single dendritic spines. Nature 429: 761–766.
35. Okamoto K, Nagai T, Miyawaki A, Hayashi Y (2004) Rapid and persistent modulation of actin dynamics regulates postsynaptic reorganization underlying bidirectional plasticity. Nat Neurosci 7: 1104–1112.
36. Korn ED, Carlier MF, Pantaloni D (1987) Actin polymerization and ATP hydrolysis. Science 238: 638–644.
37. Konishi M (1998) Cytoplasmic free concentrations of Ca^{2+} and Mg^{2+} in skeletal muscle fibers at rest and during contraction. Jpn J Physiol 48: 421–438.
38. Fukazawa Y, Saitoh Y, Ozawa F, Ohta Y, Mizuno K, et al. (2003) Hippocampal LTP is accompanied by enhanced F-actin content within the dendritic spine that is essential for late LTP maintenance in vivo. Neuron 38: 447–460.
39. Lynch MA (2004) Long-term potentiation and memory. Physiol Rev 84: 87–136.

Development/Plasticity/Repair

Microglia Enhance Neurogenesis and Oligodendrogenesis in the Early Postnatal Subventricular Zone

Yukari Shigemoto-Mogami,[1] Kazue Hoshikawa,[1] James E. Goldman,[2] Yuko Sekino,[1] and Kaoru Sato[1]

[1]Laboratory of Neuropharmacology, Division of Pharmacology, National Institute of Health Sciences, Tokyo 158-8501, Japan, and [2]Department of Pathology and Cell Biology, Columbia University College of Physicians and Surgeons, New York, New York 10032

Although microglia have long been considered as brain resident immune cells, increasing evidence suggests that they also have physiological roles in the development of the normal CNS. In this study, we found large numbers of activated microglia in the forebrain subventricular zone (SVZ) of the rat from P1 to P10. Pharmacological suppression of the activation, which produces a decrease in levels of a number of proinflammatory cytokines (i.e., IL-1β, IL-6, TNF-α, and IFN-γ) significantly inhibited neurogenesis and oligodendrogenesis in the SVZ. *In vitro* neurosphere assays reproduced the enhancement of neurogenesis and oligodendrogenesis by activated microglia and showed that the cytokines revealed the effects complementarily. These results suggest that activated microglia accumulate in the early postnatal SVZ and that they enhance neurogenesis and oligodendrogenesis via released cytokines.

Key words: cytokine; microglia; neurogenesis; neurosphere; oligodendrogenesis; subventricular zone

Introduction

CNS microglia have long been considered as resident immune cells, which are activated in response to pathological events. In pathological conditions, they change their morphology to an amoeboid shape, acquiring activation-specific phenotypes, such as chemotaxis, phagocytosis, and secretion of inflammatory cytokines (Nakajima and Kohsaka, 2001; Inoue, 2008; Monji et al., 2009; Kettenmann et al., 2011). However, microglia also have physiological roles in the normal CNS. They actively survey their territory with fine processes and receive stimuli from the environment as sensor cells (Kettenmann et al., 2011). *In vivo* lineage tracing studies have established that microglia differentiate from primitive myeloid progenitors that arise before embryonic day 8 and are identified in the CNS parenchyma even before definitive hematopoiesis (Ginhoux et al., 2010), whereas it has also been shown that microglia migrate from the lateral ventricle into the brain via the subventricular zone (SVZ) in the postnatal brain (Mohri et al., 2003). In the early embryonic brain, most microglia adopt an amoeboid morphology and characteristics of an activated form (Hirasawa et al., 2005). Microglia in the embryonic SVZ limit the production of cortical neurons by phagocytosing neural precursor cells (Cunningham et al., 2013). The number of microglia in the brain reaches a maximum during the early postnatal weeks (Wu et al., 1993; Xu and Ling, 1994), after which they transform into cells with a ramified shape, the typical morphology observed in the adult CNS (Ignácio et al., 2005). However, microglia are densely populated in neurogenic niches, such as the SVZ (Mosher et al., 2012), and appear more activated in the adult SVZ than in non-neurogenic zones (Goings et al., 2006). These developmental changes in the activation and the distribution of microglia strongly suggest that microglia play important roles in CNS development. However, the developmental dynamics of microglia in the postnatal SVZ and their roles in neurogenesis and gliogenesis at this stage are not well understood. We have examined the distribution and morphology of microglia in the rat forebrain during the neonatal-early postnatal period in detail and found a large number of active forms within the SVZ from P1 to P10, which then transformed from an activated form to a ramified form after P14. We here present evidence that microglia in the early postnatal SVZ promote both neurogenesis and oligodendrogenesis and that cytokines are important in these effects. To our knowledge, this is the first report showing a novel physiological function of microglia regulating neurogenesis and oligodendrogenesis in the early postnatal brain.

Materials and Methods

Animals and treatment. All animals were treated in accordance with the guidelines for the Care and Use of Laboratory Animals of the Animal Research Committee of the National Institute of Health Sciences and followed the *Guide for the Care and Use of Laboratory Animals*. All experiments were approved by the Animal Research Committee of National Institute of Health Sciences and conformed to the relevant regulatory standards. The Wistar rats were purchased from Japan SLC and maintained under specific pathogen-free conditions at a controlled temperature and humidity and on a 12 h light/12 h dark cycle and had *ad libitum*

Received April 15, 2013; revised Dec. 21, 2013; accepted Dec. 27, 2013.

Author contributions: K.S. designed research; Y.S.-M., K.H., and K.S. performed research; Y.S.-M., K.H., J.E.G., Y.S., and K.S. analyzed data; Y.S.-M., J.E.G., Y.S., and K.S. wrote the paper.

This work was supported in part by a Grant-in-Aid for Young Scientists from MEXT, Japan (KAKENHI 21700422), the Program for Promotion of Fundamental Studies in Health Sciences of NIBIO, Japan, a Health and Labor Science Research Grant for Research on Risks of Chemicals, a Labor Science Research Grant for Research on New Drug Development from the MHLW, Japan to K.S., and a Health and Labor Science Research Grant for Research on Publicly Essential Drugs and Medical Devices, Japan to Y.S.

The authors declare no competing financial interests.

This article is freely available online through the *J Neurosci* Author Open Choice option.

Correspondence should be addressed to Dr. Kaoru Sato, Laboratory of Neuropharmacology, Division of Pharmacology, National Institute of Health Sciences, Kamiyoga 1-18-1, Setagaya-ku, Tokyo 158-8501, Japan. E-mail: kasato@nihs.go.jp.

DOI:10.1523/JNEUROSCI.1619-13.2014

 0270-6474/14/342231-13$15.00/0

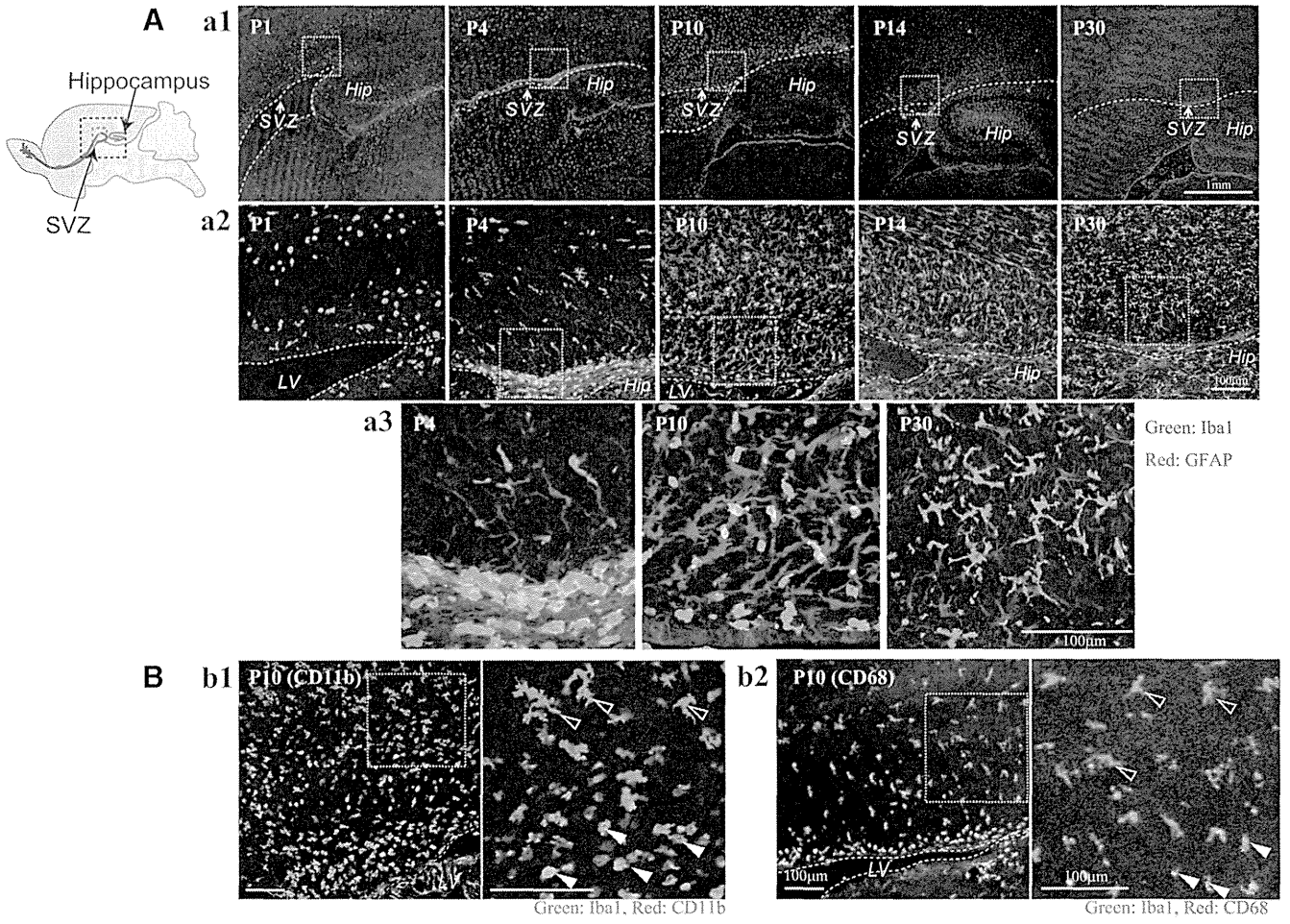

Figure 1. There is a population of activated microglia accumulated in the early postnatal SVZ. ***Aa1***, Distribution of microglia in the postnatal VZ/SVZ (P1, P4, P10, P14, P30). Sagittal sections of forebrains were immunostained with anti-Iba1 (green: microglia) and anti-GFAP antibodies (red: neural stem cells and astrocytes). ***Aa2***, Magnified images of the hatched squares in ***Aa1***. The accumulation in the SVZ in P4 and P10 was distinctive. ***Aa3***, Magnified images of the hatched squares in ***Aa2***. Morphological changes of microglia with age from amoeboid shape to more ramified shape is remarkable (P4, P10, P30). ***Bb1***, Activation of microglia in P10 SVZ. Sagittal sections immunostained with anti-CD11b (red: activated microglia) and anti-Iba1 antibodies (green: microglia). Right panel, Magnified image of the hatched square in the left panel. The microglia in the SVZ have an amoeboid shape and positive for CD11b (white arrowheads), whereas those outside SVZ have more ramified shape and are negative for CD11b (black arrowheads). ***Bb2***, Sagittal sections immunostained with anti-CD68 (red: activated microglia) and anti-Iba1 antibodies (green: microglia). Right panel, Magnified image of the hatched square in the left panel. The microglia in the SVZ have an amoeboid shape and positive for CD68 (white arrowheads), whereas those outside SVZ have more ramified shape and are negative for CD68 (black arrowheads). Similar results were obtained in three independent experiments.

access to food and water. Minocycline (30 mg/kg) or the same volume of PBS was injected into rats of either sex intraperitoneally for 3 d from postnatal day 2 (P2). Six hours after the last injection, rats were deeply anesthetized and the brains were removed on ice.

Immunohistochemistry (sagittal sections). Rats (P1, P4, P10, P14, P30) were anesthetized and then perfused with saline followed by 4% PFA, and then the brains were removed. From each half brain, sagittal sections were cut laterally at a thickness of 30 μm beginning 2 mm lateral from the midline. The sections were incubated for 2 h at room temperature in a blocking solution (3% normal goat serum, 0.3% Triton X-100 in PBS) and incubated for 24 h at 4°C in the solution, including the primary antibodies (rabbit anti-Iba1 antibody [019–9741, Wako; 1:500], mouse anti-GFAP antibody [MAB3402, Millipore; 1:200], mouse anti-rat CD11b antibody [MAB1405, AbD Serotec; 1:100], anti-rat CD68 antibody [MCA341R, AbD Serotec; 1:100], rabbit anti-Ki-67 [SP6, M3061, Spring Bioscience; 1:10], anti-nestin antibody [MAB353, Millipore; 1:100], goat anti-doublecortin [Dcx] antibody [sc-8066, Santa Cruz Biotechnology; 1:200], goat anti-PDGFRα antibody [sc-31178, Santa Cruz Biotechnology; 1:50], anti-oligodendrocyte marker O1 [O1] antibody [MAB344, Millipore, 1:50], mouse anti-MBP antibody [MAB 382, Millipore; 1:50], rabbit anti-ALDH1L1 antibody-astrocyte marker antibody [ab87117, Abcam; 1:1000], mouse anti-S100β antibody [S2532, Sigma; 1:100], rabbit anti IGF-1 antiserum [GroPep Biotechnology; [1:200]). After incubation, the sections were washed and incubated for 3 h at room temperature in the solution, including the secondary antibodies (anti-rabbit IgG-conjugated Alexa Fluorochrome or anti-mouse IgG-conjugated Alexa Fluorochrome [Invitrogen; 1:1000]). The stained sections were analyzed using a Nikon A1R-A1 confocal microscope system. To count the number of cells positive for each differentiation marker, 613 × 613 μm^2 and 1024 × 1024 μm^2 squares were set on both sides of the fornix. The cell numbers in the two squares were counted and averaged for the cell numbers in one section. The averaged data of 3 sections at 90 μm intervals were treated as the data of one animal and the data from 6 animals were statistically analyzed.

Immunohistochemistry (coronal sections). Three points on the skull at three different rostrocaudal stereotaxic coordinates (i.e., anterior, middle, posterior) were marked with animal tattoo ink (Ketchum) at P1. These three points with different rostrocaudal levels were determined according to a previous report (Suzuki and Goldman, 2003): rostral point: 2 mm anterior, 1 mm lateral to the bregma; middle point: 0.7 mm anterior, 1 mm lateral to the bregma; caudal point: 0.5 mm posterior, 1 mm lateral to the bregma. Then the animals were perfused at P1, P3, P10, and P30, and the brains were removed as described above. From each half brain, coronal sections were cut at each marked point from anterior to posterior. The sections were immunostained with anti-Iba1 and anti-CD68 as described above. After immunostaining, the sections were coun-

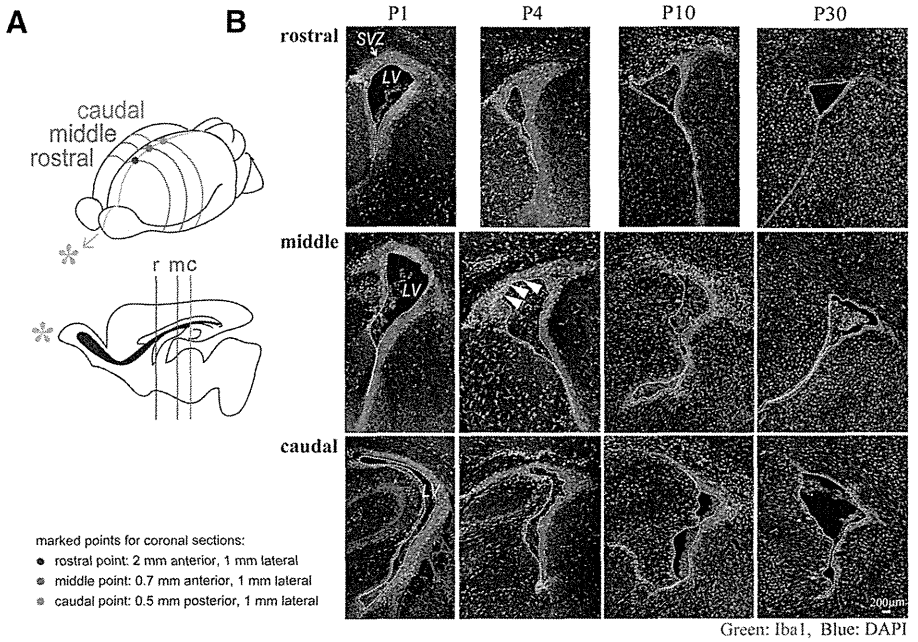
A
B
caudal
middle
rostral
r mc
marked points for coronal sections:
rostral point: 2 mm anterior, 1 mm lateral
middle point: 0.7 mm anterior, 1 mm lateral
caudal point: 0.5 mm posterior, 1 mm lateral
P1
P4
P10
P30
rostral
middle
caudal
SVZ
LV
200μm
Green: Iba1, Blue: DAPI

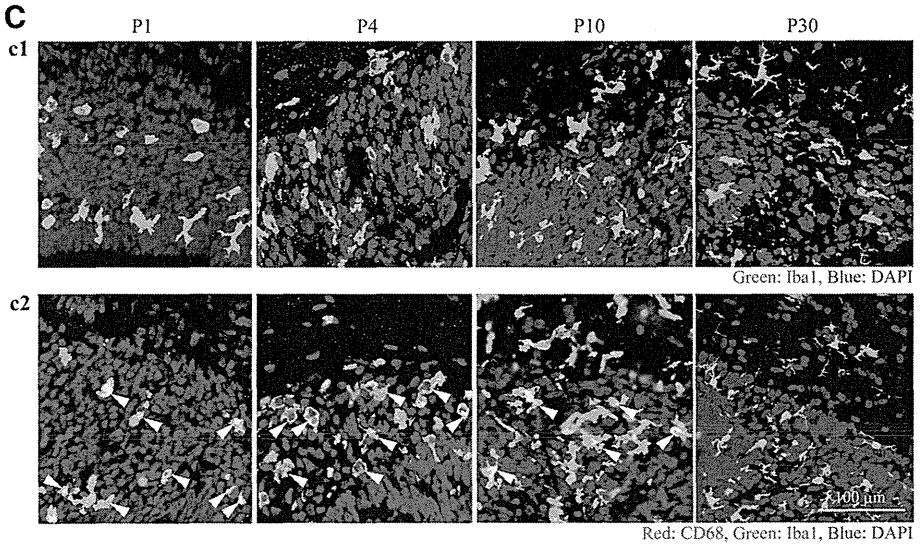
C
P1
P4
P10
P30
c1
Green: Iba1, Blue: DAPI
c2
100 μm
Red: CD68, Green: Iba1, Blue: DAPI

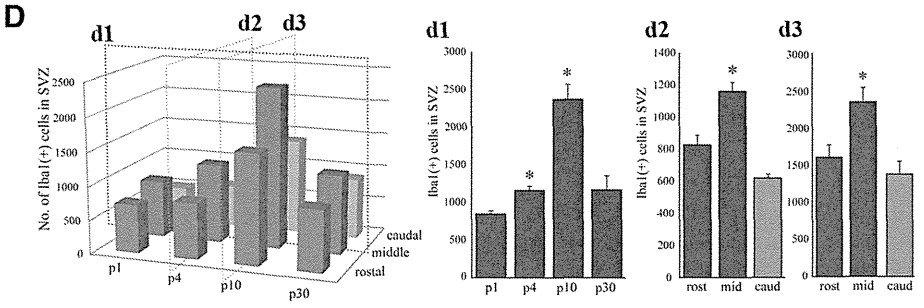
D
d1
d2
d3
No. of Iba1(+) cells in SVZ
caudal
middle
rostral
p1
p4
p10
p30
Iba1(+) cells in SVZ
rost
mid
caud

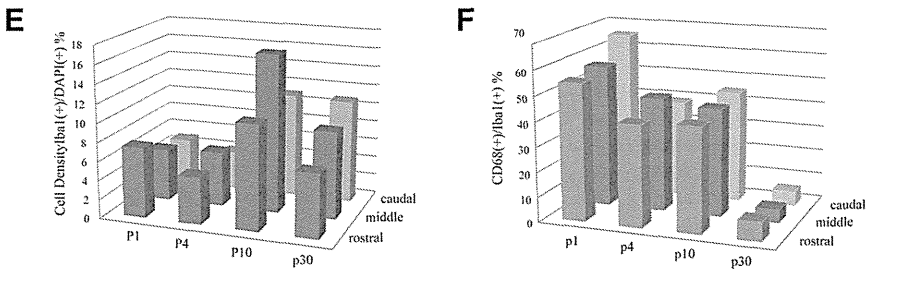
E
F
Cell Density(Iba1(+)/DAPI(+) %
CD68(+)/Iba1(+) %
caudal
middle
rostral
P1
P4
P10
p30

terstained with DAPI (1:500; Invitrogen) for 30 min to visualize the SVZ. The cell numbers of microglia (Iba1 $^+$) and activated microglia (Iba1 $^+$ CD68 $^+$) in the SVZ (the region with dense DAPI signals) were counted in one section. The averaged data of three sections at 90 μm intervals across the marked points were treated as the data for each rostrocaudal level. The data from 6 to 9 hemispheres per one rostrocaudal level were statistically analyzed.

Western blotting. P4 Wistar rat brains were cut into sagittal sections. Under a microscope, a parasagittal section (from 1 mm lateral, 2 mm thickness) was taken from each half brain and meninges were carefully removed. The VZ/SVZ was identified by its slightly darker, more transparent appearance compared with the overlying corpus callosum. We cut out the VZ/SVZ between 0.4 mm anterior and 3 mm posterior (posterior end of SVZ) from bregma so as not to include the rostral migratory stream. Dissected VZ/SVZ tissues were homogenized on ice in extraction buffer (20 mM Tris, 2 mM EDTA, 0.5 mM EGTA, 0.32 M sucrose, protease inhibitor mixture), and centrifuged at 1000 × *g* for 10 min. Proteins in the lysates were resolved with SDS-PAGE and transferred to PVDF membranes. The membranes were incubated overnight in BlockAce blocking solution at 4°C. Then the membranes were incubated with primary antibodies (anti-CD11b [1:1000], anti-CD68 [1:2000], anti-nestin [1:1000], anti-PDGFRα [1:200], anti-ALDH1L1 [1:1000], anti-S100β [1:2000]) for 1 h at 25°C. After washing three times, the membranes were incubated with HRP-conjugated anti-rabbit or anti-mouse antibody (1:5000) for 1 h at 25°C. The membranes were then washed three times and signals were visualized by chemiluminescence detectors LAS3000 (Fuji film).

Measurement of cytokine levels. Cytokine levels in the SVZ were determined with Bio-Plex cytokine analysis system (Bio-Rad Laboratories). Tissue lysates of VZ/SVZ fractions were obtained from rats at P1, P4, P10, and P30 as described in Western blotting. The concentrations of Il-1α, Il-1β, IL-2, IL-4, IL-6, Il-10, GM-CSF, IFN-γ, and TNF-α were measured by the Bio-Plex rat cytokine 9 plex kit according to the manufacturer's instruction. In some cases, IGF-1, Il-1β IL-6, TNF-α, and IFN-γ concentrations were measured by ELISA kit according to the manufacturer's instruction. The protein levels of tissue lysates were measured by BCA protein assay. The amount of each cytokine in 100 μg of total protein is shown for comparison. To determine the cytokine release from activated microglia *in vitro*, microglia were activated by LPS (10 ng/ml) in the presence or absence of minocycline (10 μM) for 30 min and washed carefully and incubated in the normal medium for 24 h. After 24 h incubation, the cell culture supernatants were collected, and concentration of Il-1β, IL-6, IFN-γ, and TNF-α were measured by ELISA kit.

Cell culture: neurosphere culture. Rat neural stem cells were cultured as previously described (Reynolds et al., 1992; Hamanoue et al., 2009) with slight modifications. Briefly, telencephalons were dissected from embryonic day 16 (E16) rats of either sex in ice-cold DMEM/F12, minced, and dispersed into single cells by pipetting. Cells were then cultured in DMEM/F12 containing B27 supplement (×200), 20 ng/ml FGF2, and 20 ng/ml EGF for 7 d. The primary neurospheres and single cells were differentiated in growth factor-free medium in glass chambers coated with ornithine/fibronectin. In some cases, primary neurosphere were incubated with TrypLE Select for 15 min and dissociated by pipetting. Single cells were differentiated in glass chambers coated with polyornithine/laminin.

Microglia culture. Rat microglia were cultured as previously described (Nakajima et al., 1992). In brief, mixed glial cultures were prepared from the cerebral cortex of P1 Wistar rats and maintained for 12–23 d in DMEM containing 10% FBS. The floating microglia over the mixed glial cultures were collected and transferred to appropriate dishes or transwells.

Neural stem cell differentiation assay. To examine the effects of activated microglia on neural development and the contribution of cytokines to the effects, we used modified cocultures of neurospheres with activated microglia. Microglia cultured independently of neurospheres on transwells were activated by LPS (10 ng/ml) in the presence or absence of minocycline (10 μM) for 30 min and washed carefully to prevent residual LPS and minocycline. The transwells on which microglia were cultured were set on the neurospheres 1 d after the starting point of the differentiation and incubated for differentiation periods suitable for neurons (7 d) or oligodendrocytes (11 d). In some cases, we performed the coculture of cells dissociated from neurospheres and activated microglia. To check the effects of minocycline alone, these cells were incubated in the presence of minocycline (10 μM) for 7 d. Neurospheres and single neural stem cells were immunohistochemically stained for β3-tubulin, PDGFRα, O4, GFAP, and TOTO3 according to the manufacture's instruction (Stem Cell Kits, R&D Systems). To examine the effects of function-blocking antibodies on differentiation, the neurospheres were differentiated in the presence of function-blocking antibodies (goat anti-rat IL-1β antibody [AF-501-NA, R&D Systems], goat anti-rat IL-6 antibody [AF-506, R&D Systems], TNF-α antibody [70R-TR007X, Fitzgerald], and goat anti-mouse/rat IFN-γ antibody [AF-585-NA, R&D Systems]) (1 μg/ml for each). The effects of these function-blocking antibodies were compared with the same concentration of isotype-matched control IgG: normal goat IgG control [AB-108-C, R&D Systems] and rabbit IgG control [31R-AR001, R&D Systems] (1 μg/ml for each). The effect of the mixture of function blocking antibodies (goat anti-rat IL-1β antibody, goat anti-rat IL-6 antibody, TNF-α antibody, and goat anti-mouse/rat IFN-γ antibody, 1 μg/ml for each) was compared with the control, which included same concentrations of isotype-matched control IgGs (i.e., 3 μg/ml of normal goat IgG control and 1 μg/ml of rabbit IgG control). To examine the effects of a single cytokine, the neurospheres were differentiated in the presence of each individual recombinant cytokine (rIL-1β, rIL-6, rTNF-α, and rIFN-γ at 1 or 10 ng/ml). After the differentiation period, the cells were stained immunocytochemically as described above.

Data analysis and statistics. All data are shown as the mean ± SEM. Statistical analysis was performed using Student's *t* test, or Tukey's test by ANOVA. Differences were considered to be significant at $p < 0.05$.

Materials. Minocycline, LPS, anti-S100β antibody (S2532), and EGF were purchased from Sigma. Bio-Plex rat cytokine 9 plex was purchased from Bio-Rad Laboratories. Recombinant cytokines (rIL-1β, rIL-4, rIL-6, rIFN-γ, rTNF-α) and FGF2 were purchased from PeproTech. Maximum sensitivity substrate and BCA protein assay were purchased from Thermo Scientific. CanGet Signals was purchased from Toyobo. HRP-conjugated anti-rabbit, mouse antibodies were purchased from GE Healthcare Life Science. DAPI, TOTO3, anti-mouse, sheep, rabbit IgG, and anti-mouse IgM-conjugated AlexaFluor were purchased from Invitrogen. BlockAce was purchased from DS Pharma Biomedical. B27 supplement, TrypLE Serect, FBS, and DMEM were purchased from Invitrogen.

Results

We first investigated the distribution of microglia in the postnatal rat forebrain (Figs. 1 and 2). Sagittal sections were immuno-

←

Figure 2. The temporal and spatial dynamics of activated microglia in the postnatal SVZ. ***A***, A schematic of the rostrocaudal levels in this experiment. ***B***, The distribution of microglia in the rostral, medial, and caudal SVZ at P1, P4, P10, and P30. Coronal sections of forebrains at rostral (2 mm anterior to the bregma), medial (0.7 mm anterior to the bregma), and caudal (0.5 mm posterior to the bregma) levels were immunostained with anti-Iba1 (green: microglia) followed by DAPI staining (blue: cell nuclei). A population of activated microglia accumulated within the SVZ at P1-P10. ***Cc1***, Typical morphology of microglia in the middle SVZ at P1, P4, P10, and P30. Morphological change of microglia with age from amoeboid shape to more ramified shape is remarkable. ***Cc2***, The middle SVZ sections immunostained with anti-CD68 (red: activated microglia) and anti-Iba1 antibodies (green: microglia). The microglia at P1, P4, and P10 in the SVZ have an amoeboid shape and are positive for CD68 (representative cells: white arrowheads), whereas those at p30 have a more ramified shape and are negative for CD68. ***D***, The quantification of the number of Iba1 $^+$ cells in the SVZ. ***d1***, Time course of the Iba1 $^+$ microglia in the middle SVZ. The number peaked at P10. d2, d3, The comparison of the numbers of microglia among the rostral, middle, and caudal SVZ at P4 (***d2***) and P10 (***d3***). *$p < 0.05$ versus p1 or rost group (Tukey's test by ANOVA). Data are mean ± SEM. ***E***, The cell density of Iba1 $^+$ microglia at different rostrocaudal levels at P1, P4, P10, and P30. The cell density of microglia in the SVZ paralleled with that of the number of microglia throughout a period of the observation. ***F***, The ratio of activated microglia in the SVZ (CD68 $^+$/Iba1 $^+$). During the experimental period, the highest ratio was obtained at P1. We confirmed the similar results in three independent experiments.

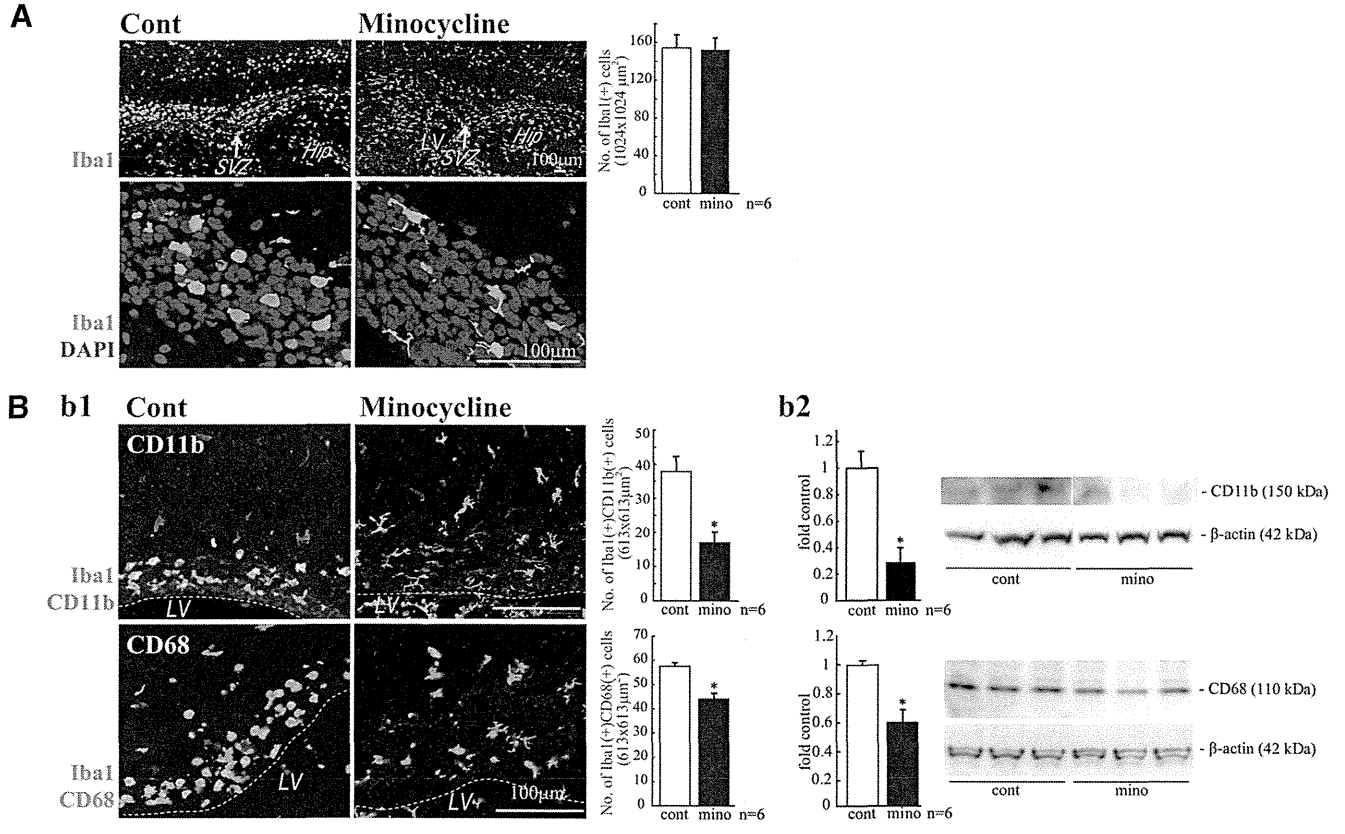

Figure 3. Minocycline suppressed microglial activation *in vivo*. ***A***, Effects of minocycline on the number of Iba1 $^{+}$ cells in the SVZ and their morphologies. Minocycline was administered by intraperitoneal injection for 3 d beginning at P2 (30 mg/kg/d, P2-P4, $n = 6$/group). Sagittal sections of minocycline-treated forebrains were immunostained for Iba1 (green) followed by DAPI staining (cyan). Although the number of Iba1 $^{+}$ microglia in the SVZ did not change (graph), their shape shifted from an amoeboid type to a more ramified type by minocycline (bottom). ***Bb1***, Effects of minocycline on the expression of activation markers and the morphologies of microglia. Sagittal sections of minocycline-treated forebrains were immunostained for Iba1 (green), and CD11b (red), and CD68 (red). Minocycline significantly decreased the number of cells positive for CD11b or CD68. The morphologies of the cells were also changed from amoeboid shape to more ramified shape. ***Bb2***, The significant decrease in the expression of CD11b and CD68 was confirmed by Western blotting of the SVZ as well. $^{*}p < 0.05$ (Student's t test). Data are mean ± SEM. Similar results were obtained in three independent experiments.

stained with anti-Iba1, the marker for all microglia (green: microglia), and anti-GFAP antibodies (red: neural stem cells and astrocytes) at P1, P4, P10, P14, and P30. We found that a large number of microglia accumulated in the postnatal SVZ from P1 to P10 (Fig. 1*A*), especially at P4. The microglia in the VZ/SVZ at P1 and P4 display an amoeboid shape, whereas those outside the SVZ have a more ramified shape (Fig. 1*Aa2*). At P10, the number of microglia outside the SVZ had dramatically increased; the microglia in the VZ/SVZ remained amoeboid. At P14, the number of microglia had increased further and now ramified microglia were also observed in the VZ/SVZ. At P30, the numbers of microglia in the SVZ had decreased and most of the microglia had assumed a ramified shape. Further magnified images in Figure 1*Aa3* show that the shape of microglia in the SVZ changed gradually from amoeboid (P4) to ramified (P30). Figure 1*B* shows the expression of CD11b (Fig. 1*Bb1*) and CD68 (Fig. 1*Bb2*) in the SVZ microglia at P10. CD11b is potentially a marker for all microglia; however, its level is highly elevated by activation. CD68 is a marker for activated microglia. The levels of CD11b and CD68 are much higher in the amoeboid microglia in the SVZ (white arrowheads) than in the ramified ones outside the SVZ (black arrowheads), indicating that the SVZ amoeboid microglia have an activated phenotype.

To examine the developmental dynamics of microglia in the SVZ temporally and spatially, we examined the distribution of microglia in coronal sections that include rostral, medial, and caudal SVZ at P1, P4, P10, and P30 (Fig. 2). Each rostrocaudal level was determined according to a previous report (Suzuki and Goldman, 2003). Coronal sections were immunostained with anti-Iba1 (green: microglia) followed by DAPI staining (blue: cell nuclei) (Fig. 2*B*,*C*). The SVZ could be clearly delineated by its dense cellularity. From P1 to P10, a large number of microglia accumulated at all rostral, middle, and caudal levels. When we quantified the number of microglia in the SVZ, they gradually increased from P1 to P10, reached a maximum at p10, and decreased at P30 at all coronal levels (Fig. 2*B*,*D*, d1). Microglia displayed an amoeboid shape at P1, P4, and P10 but had become more ramified at P30 (Fig. 2*Cc1*). Among the different rostrocaudal levels, the number of microglia in the middle SVZ was significantly larger than in other levels at all ages (Fig. 2*D*, d2, d3). The changes in cell density (i.e., the ratio of Iba1 $^{+}$/DAPI $^{+}$) of microglia in the SVZ paralleled that of the number of microglia throughout the period of observation (Fig. 2*E*). We next examined immunostaining for CD68 in SVZ microglia. Figure 2*Cc2* shows representative images of double staining with anti-Iba1 and anti-CD68. At P1 and P4, most Iba1+ microglia in the SVZ were also positive for CD68. At P4, the CD68 signals became much stronger. At P10, a few microglia had appeared that had little CD68. At P30, double-positive cells were markedly decreased in number. The time course of the ratio of CD68 $^{+}$/Iba1 $^{+}$ cells is shown in Figure 2*F*: the highest ratio was obtained at P1. The ratios at P4 and P10 were almost equivalent and then were

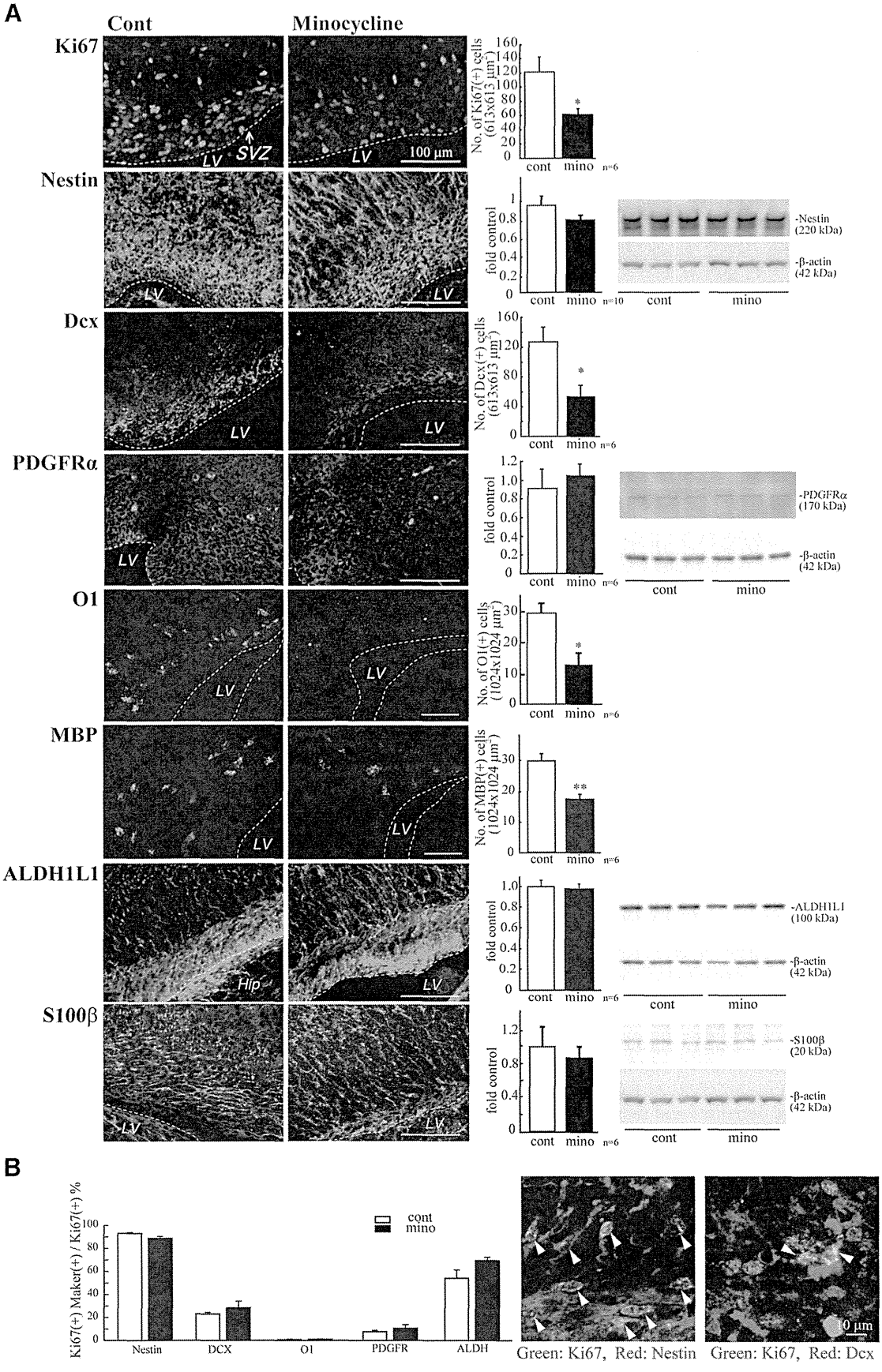

Figure 4. Minocycline decreased the numbers of proliferating cells, neuronal progenitors, and oligodendrocyte progenitors in the early postnatal SVZ. ***A***, Minocycline was administered by intraperitoneal injection for 3 d beginning at P2 (30 mg/kg/d, P2-P4, $n = 6$/group). Sagittal sections of forebrains were immunostained with antibodies to Ki67, nestin, Dcx, PDGFRα, O1, MBP, ALDH1L1, and S100β. The numbers of cells positive for Ki67, Dcx, MBP, or O1 were counted, whereas the protein levels of nestin, PDGFRα, ALDH1L1, and S100β (*Figure legend continues.*)